STRESS ANALYSIS AND MODELING OF A MICROCHANNEL REACTOR FOR FISCHER-TROPSCH SYNTHESIS

by

Rajan Bhaskarrai Kher

BE Chemical Engineering, Gujarat Technological University, 2014

Submitted to the Graduate Faculty of

Swanson School of Engineering in partial fulfillment

of the requirements for the degree of

Master of Science in Chemical Engineering

Master of Science in Petroleum Engineering

University of Pittsburgh

2018

UNIVERSITY OF PITTSBURGH

SWANSON SCHOOL OF ENGINEERING

This thesis was presented

by

Rajan Bhaskarrai Kher

It was defended on

April 9, 2018

and approved by

George E. Klinzing, Ph.D., Professor
Department of Chemical and Petroleum Engineering

Robert M. Enick, Ph.D., Professor
Department of Chemical and Petroleum Engineering

Thesis Advisor: Badie I. Morsi, ScD, Professor
Department of Chemical and Petroleum Engineering

STRESS ANALYSIS AND MODELING OF A MICROCHANNEL REACTOR FOR FISCHER-TROPSCH SYNTHESIS

Rajan Bhaskarrai Kher, M.S

University of Pittsburgh, 2018

The main objective of this research is to conduct stress analysis calculations and modeling of a MCR for Fischer-Tropsch (F-T) synthesis with the aim to build an optimized lab-scale micro-channel reactor (MCR) in our laboratory. 2-D and 3-D models were used for stress analysis calculations in a MCR containing 10 channels and provided with two 10-mm diameter hole for gas entrance and exit. The analyses, including total deformations, von Mises stresses and principal stresses, were calculated with ANSYS using the Finite Element Method. Two different construction materials for the MCR, namely Plexiglas and 316 Stainless Steel were considered in the calculations. Also, a 2-D pseudo-homogeneous dispersion model was built in MATLAB to investigate F-T synthesis using cobalt catalyst in the MCR. The effects of superficial syngas velocity and H_2/CO ratios on the CO conversion were investigated. This study led to the following conclusions:

1. The 2-D stress analysis model predicted the failure of the MCR inlet surface by evaluating the elastic plastic fracture mechanics of the structure. The 3-D stress analysis showed that the maximum stresses exhibited within the structure were generally lower than the maximum yield strength of both Plexiglas and Stainless steel.

2. Increasing the inlet superficial gas velocity decreased the CO conversion and the temperature distribution in the MCR. The highest CO conversion and temperature values were exhibited at the centerline of the reactor. The temperature gradients decreased significantly with increasing

superficial gas velocity. Decreasing the H_2/CO ratio of the feed systematically decreased the CO conversion throughout the packed-channel, whereas increasing the H_2/CO ratio resulted in higher and steeper CO conversion contours. The hydrocarbons yield was determined to be 3.84 bbl/day for 3600 channels with dimensions of 4 mm x 4 mm x 150 mm operating at P = 25 bar, T = 483 K, H_2/CO ratio of 2, and a superficial inlet velocity of 0.05 m/s, the yield was also determined to be 4.24 bbl/day when operating at a superficial velocity of 0.01 m/s.

TABLE OF CONTENTS

LIST OF TABLES

LIST OF FIGURES

ACKNOWLEDGMENT

NOMENCLATURE

a	Channel cross-sectional area, m^2
D^{axial}	Axial dispersion coefficient, m^2/s
$D^{lateral}$	Lateral dispersion coefficient, m^2/s
d_h	Hydraulic diameter, m
d_p	Catalyst diameter, m
E	Young's Modulus, Pa or psi
g	gravity, m·s^{-2}
K	Stress concentration factor, -
L	Length of Bed, m
P	Pressure, Pa
R	Gas constant, J mol^{-1}K^{-1}
Re	Reynolds number, -
T	Temperature, K
u	superficial gas velocity, m·s^{-1}
E$_{FT}$	Activation energy J mol^{-1}
^{k}FT	Fischer Tropsch reaction rate coefficient kmol kg$_{cat}^{-1}$s^{-1}Pa^{-1}

Greek Symbols

α	Gas or liquid phase
β	Liquid phase
ε	Volume fraction of the phase, -
ν	Poisson's ratio, -
ϵ	Strain, (m/m)
ρ	Density, $kg.m^{-3}$
σ_n	First principal stress, $Pa.m^{-2}$
σ_{yp}	Yield point of the material, Pa or psi
σ_{nom}	Nominal stress
τ	Shear stress, $Pa.m^{-2}$

Acronyms

MCR	Micro channel Reactor
FEA	Finite element Analysis
FEM	Finite element Method
APDL	Ansys parametric design language
GTL	Gas to Liquid
CTL	Coal-to-liquid
EOS	Equation-of-state
PBR	Packed-bed reactor

1.0   INTRODUCTION

1.1 PROCESS INTENSIFICATION

Over the past decade, significant work has been carried out in investigating process intensification, with focus on modular reactors technology (MRT) and catalysts, which has been led by growing technology companies like Velocys and CompactGTL, among others. Efforts in understanding, optimizing and commercializing MRT technology are still very much at their infancy, however, the recent success of Velocys' ENVIA Energy demonstration plant in Oklahoma [1] has increased confidence in the potential of using MRT. The motivation of this approach lies in the fact that the main components of a given plant, such as reactors, heat exchangers, separators, etc., only represent about 20% of the overall capital cost, whereas 80% of the cost is incurred by installation and commissioning, which includes pipe-study, structural support, civil engineering, etc. [15]. This means that major reductions in the equipment size, coupled preferably with a degree of telescoping of equipment function, such as reactor/heat exchanger unit, or combined distillation/condenser/re-boiler, could result in significant cost savings by eliminating the support structure, expensive foundations and long pipe runs.

Moreover, process intensification enables efficient integration of thermal and mass transport operations and minimizes operating variable gradients within the system, while minimizing financial risk of deployment. In general, the transport fluxes of mass, energy and momentum are dependent, not only on the mass diffusivity, thermal conductivity and viscosity,

but also, on the corresponding concentration, temperature, and velocity gradients. The decrease of the physical dimensions (miniaturization) of a unit operation leads to the enhancement of mixing and heat exchange, which increase the mass and heat transfer rates as well as the viscous losses [2, 3]. Also, with miniaturization, the amount of material in a system is reduced, and the surface area per unit volume is increased. Thus, miniaturization leads to high mass and heat transfer rates per unit volume while exploiting the underlying catalyst potential, however, the effect of viscous losses has to be taken into account [4, 5]. Such advantages, when coupled with potential capital and operating costs of up to 60% [6, 7], make MRT an exciting prospect to fill very lucrative market gap in the petrochemical and chemical production industries. As a matter of fact, these reactors have been used in the following processes: (1) F-T synthesis [8-11]; (2) Biomass-to-Liquid [12]; (3) Water-Gas-Shift (WGS) reaction [13]; (4) Methanol Steam Reforming [14, 15]) (5) H_2/O_2 Combustion [16]; (6) Gas-Phase Partial Oxidation [17]; (7) Selective Oxidation [18]; (8) Catalytic Partial Oxidation [19] and (9) Nitration of o-Nitrotoluene [20]. Table 1 provides a summary of previous investigations of MCRs.

Table 1: Experimental investigation in micro-channel reactors

Reference	Process Studied	Reactor Dimensions/ System investigated
Pfeifer et al. (2003) [21]	Electrically heated micro-reactor with channel depth of 100 μm and channel width of 100 μm, and overall channel volume of 20 cm^3.	Investigated reaction conversions, temperature gradients along the reactor and startup times.
Nemec et al. (2005) [22]	A model prediction of pressure drop and liquid holdup for trickling flow in packed Bed reactors has been developed based on the relative permeability concept. The proposed model was able to predict liquid holdup and pressure drop to within 5 % and 20 % respectively, regardless of type of packing or operating ranges investigated in this model	Effect of gas flow rate on liquid phase relative permeability at 10 bar total pressure for bed of 1.41-mm catalyst particles
Ge et al. (2005) [17]	Measured the effect of temperature and space velocity on reaction conversion and selectivity on the gas phase partial oxidation of toluene over V/Ti catalyst beds.	Square packed bed channels with cross-sectional area: 1 mm². Catalyst particles with: d_p (μm): 300-600
Schmidt et al. (2005) [23]	Investigated the suitability of microchannel for kinetic measurements, studied the effect of temperature, pressure and channel diameter on the conversion and mass transfer parameters.	The selective oxidation of isoprene to citraconic anhydride
Karim,et al. (2005) [15]	Methanol Steam Reforming reactions were performed in catalyst packed bed and wall coated micro reactors in order to compare the performance of both configurations.	Packed Bed Channels with ID (mm): 4.1, 1.75 and 1. Catalyst loading (mg): 100, 50 and 30. Catalyst particle diameter (μm): 100–250
Aartun, et al. (2005) [19]	The partial oxidation of methane and the oxidative steam reforming of propane for the production of hydrogen or syngas were studied. The influence of the temperature distribution and the change in residence time were analyzed regarding their effect in conversion and products selectivity.	3 Fe/Cr alloy metallic reactors were used. Reactors dimension (H × W × L): 5.5 mm x 5.6 mm x 10 mm. The number of channels was 676 for two configurations and 572 for the third. Rectangular channels of 120 × 130 and 100 × 120 μm. Porosity varied from 0.22 to 0.34. Channels were impregnated with Rh in most of the cases.

Table 1 (continued).

Reference	Process Studied	Reactor Dimensions/ System investigated
Walter et al. (2005) [24]	Three different types of reactors were evaluated using the catalytic selective oxidation of isoprene as a model reaction. The performance of a ceramic fixed bed reactor, metal micro-channel reactor and a ceramic micro-channel reactor was compared.	The metal reactor was forms by six aluminum plates of 40 mm × 40 mm × 0.5 mm each. The outer dimensions were 70 mm × 70 mm × 15 mm. Channels had an inner diameter of 280 μm and were 20 mm long. The ceramic micro-reactor had an outer dimensions of 26 mm × 70 mm × 8 mm, with 16 micro-channels of square cross section (500 μm × 500 μm).
Veser (2005) [25]	Catalytic partial oxidation of methane to form synthetic gas was studied using two models of heat integrated micro-reactors. The configurations studied were counter current heat exchange reactor (CCHR) and reverse flow reactor (RFR). Syngas yields were measured and compared with a reactor without heat integration. Temperature profiles, reaction yields vs. inlet flow rate and catalyst deactivation times were also analyzed for both models.	The CCHR was formed by three concentric stainless steel tubes with an outer diameter of 25 mm and a length of 50 cm (Friedle & Veser, 1999). The RFR has a monolith structure with a 110 mm length.
Flögel et al. (2006) [26]	The synthesis of peptides was evaluated using a silicon microchannel technology. Its performance was compared with typical synthesis processes as solution phase and solid phase couplings.	Total reaction volume was 78.3 μL with a mixing zone of 9.5 μL and a Reaction loop of 68.8 μL.
Halder et al. (2007) [27]	An experimental study of the nitration of toluene in microchannel structures was carried out. The influence of the reaction temperature, acid concentration, and residence time in the production of nitro toluene was evaluated.	Stainless steel reactor with an inner diameter of 775 μm. Channels were packed with catalyst up to a packing length of 6.0 cm. The total length of the reactor was 8.0 cm. Catalyst particle diameter was between 75- 150 μm.
Men et al. (2009) [28]	Micro-channels coated with different types of catalyst were used to study the complete combustion of propane. Pt, Pd and Rh based catalysts were used for the reactions. Reaction temperature was varied. The propane conversion was evaluated over time for the different reactions conditions.	The microchannels were formed by the union of two etched plates. The openings created by these plates measure 25 mm long, 500 μm wide and 250 μm deep.

Table 1 (continued).

Reference	Process Studied	Reactor Dimensions/ System investigated
Myrstad et al. (2006) [29]	A micro structured F-T reactor was used to study the productivity, selectivity, and pressure drop and temperature profile for F-T synthesis using a Co-Re/Al$_2$O$_3$ catalyst bed. Results were compared to a laboratory scale fixed bed reactor operated at similar conditions.	2 cm^3 reactor with and 8 parallel catalyst sections of 400 μm of deep and 800 μm of height. d_p (μm): 53-75
Cao et al. (2009) [8]	A microchannel reactor system with active heat exchanger was used. The catalytic portion of the reactor is a microchannel slot with the gap width of 0.508 mm. The catalyst is located in the lower portion of the channel so that the reactants can be preheated to a desired temperature in the upper portion of the channel before entering the catalyst bed. The microchannel was sandwiched between two separated oil heating channels, which were designed to allow oil to circulate at a high rate and maintain a high heat transfer coefficient at the same time.	Packed bed Channels with packing dimension equal to 1.27 cm × 0.0508 cm ×1.778 cm. Fischer Tropsch Synthesis over two Co-Re/Al$_2$O$_3$ catalyst with different particle sizes of 150 and 45 μm. Catalyst surface area: 60 m^2/g
Deshmukh et al. (2010) [30]	The scale up capacity of microchannel reactors for F-T synthesis was studied using single channel micro reactors and multiple channel microreactors. In total four microchannel reactors were tested. The operational capacity was compared in terms of CO conversion, selectivity to secondary products and product distribution. The operational conditions of the microreactors were varied in order to test the flexibility to pressure, temperature and feed composition change.	Dimensions are in (Depth x Width x Length) / Reactor 1: Single channel (1 mm × 0.8 cm × 7 cm) + packed bed of 3.8 cm long. / Reactor 2: Single channel with two gaps. 1st gap (1 mm deep), 2nd gap: (0.5 mm deep), width – 0.6 cm, packed bed length – 61.6 cm. / Reactor 3: Similar dimensions to reactor 2. One process channels and two cooling channels / Reactor 4: 276 process channels (1 mm × 0.3 cm × 19 cm) + packed bed length: 17.1 cm. Crossflow configuration with cooling channels.
Knochen et al. (2010) [10]	The catalyst used in this study consisted of approx. 19 wt. % Co and 1 wt. % Re on Al2O3. Reaction rate measurements were carried out with a catalyst sieve fraction of 140-200 m. The 1/8" milli structured capillary reactor with 1.753 mm inner diameter had a preheating zone of 0.5 m length and a catalyst packing height of 1.0 m. A packing porosity of 33.5% was calculated from the measured apparent density of the catalyst particles.	Measured pressure drop, conversion and liquid holdup. Under typical FTS conditions the pressure drop did not exceed 1.5 bar/m at operating pressures of 20 bar, respectively. Average liquid holdup of about 2.5% was determined.
Piermartini et al. (2011) [13]	Measured the reaction conversion and selectivities at different temperatures.	Micro-structured foil stack with channel width of 200 μm, channel height of 200 μm. WGS reaction over Pt/CeO$_2$ and Pt/CeO$_2$/Al$_2$O$_3$.

Table 1 (continued).

Reference	Process Studied	Reactor Dimensions/ System investigated
Su et al. (2011) [20]	Compared the reaction kinetics and Nitro-toluene solubility in both packed and non-packed microchannels.	600 μm × 600 μm × 60 mm microchannel Nitration of o-Nitrotoluene (NT) with mixed acid.
Knobloch et al. (2013) [11]	Measured the pressure drop and liquid holdup without reaction. Determined that the pressure drop is directly proportional to the gas flow rate, therefore the kinetic term of the Ergun equation can be neglected. Observed that the pressure drop in the milli-packed-bed reactor remains moderate (2.9 bar/m)if catalyst particles with proper size and shape are employed, liquid holdup was found to be about 3%, independent of the conversion, reaction temperature, liquid hydrocarbon productivity and the reaction rate.	Low temperature Fischer Tropsch synthesis over four different Co-Re/Y-Al$_2$O$_3$ Catalyst with comparable composition and different particle shapes and sizes of 60-580 μm
Penniall (2013) [12]	Measured reaction selectivities and product yields on different catalysts.	50 channels of 37 mm length with 0.2 mm height and 0.3 mm width. BTL Fuel Plants in the New Zealand wood processing industry.
Piermantini and Pfeifer (2015) [31]	The enhancement of the CO/H$_2$ ratio of a biomass derived syngas was achieved through high temperature and pressure water gas shift reaction in a micro reactor. The reactor was tested with packed bed catalysts and with catalyst coated walls. A scale up model based on experimental and simulations results was presented.	Fixed-bed configuration: 2 foils (150 mm long, 25 mm wide) with 1029 channels each. Channels dimensions (800 μm wide, 400 μm long, and 800 μm deep). Coated walls configuration: 14 foils (150 mm long, 25 mm wide) with 50 channels each. Channels dimensions 200 μm wide, 200 μm long, and 100 μm deep).

This work is concerned with the design and modeling of a MCR for Fischer-Tropsch (F-T). The use of MCR for F-T synthesis could have a significant commercial potential, primarily due to the fact that at least 50,000 barrel per day (bpd) production F-T plant is required in order to lower the capital cost per barrel of daily capacity to an acceptable level [27, 28]. However, such large F-T plants would require about 50 MMSCF/d of feed gas, or 5.4 trillion cubic feet over a thirty year period, which limits their potential installation to only about 2% of the known gas fields outside of North America [6]. Furthermore, many other applications, such as emulsion processing, biofuels, hydro-processing and biogas conversion could also greatly benefit from compact and modular conversion technology.

A general layout of a microchannel reactor is schematically depicted in Figure 1. This type of reactor is characterized by a parallel array of vertical microchannels and cross-flow horizontal cooling microchannels. The typical dimensions of the channels are between 0.1 and 5.0 mm [32].
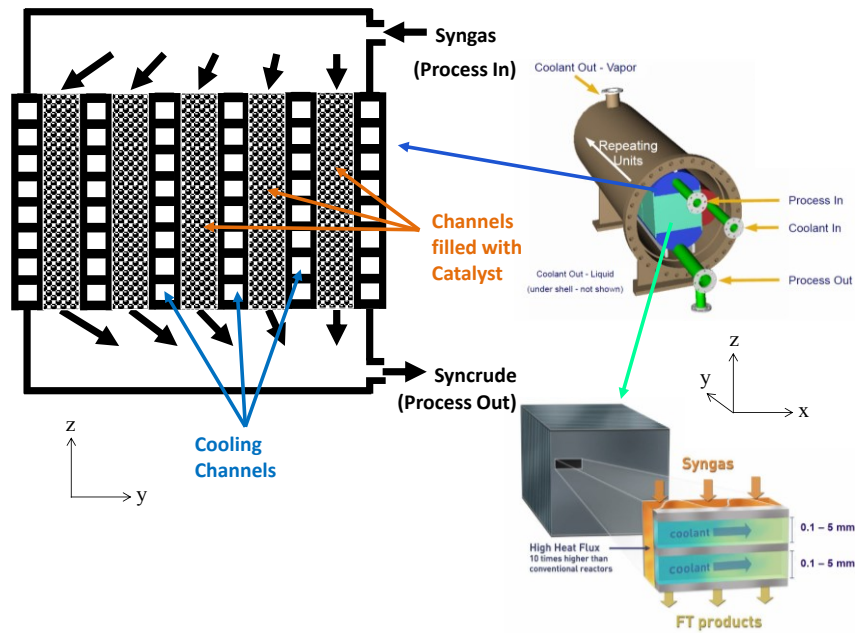
Figure 1: Application of Microchannel Reactors in F-T Synthesis by Velocys [1, 32-34]

1.2 FISCHER TROPSCH SYNTHESIS AND REACTORS

The F-T synthesis process was originally developed by Franz Fischer and Hans Tropsch in the 1920's in an effort to produce liquid fuels, based on the 1902 discovery by Sabatier and Sanders [19], that methane can be produced from H_2/CO mixtures over a nickel catalyst. It was a breakthrough in the conversion of coal to liquid fuel, such as kerosene and naphtha, and has been subsequently heavily investigated and developed commercially [20].

In F-T synthesis, CO and H_2 (syngas) react in the presence of a catalyst, conventionally iron or cobalt, to produce synthetic hydrocarbon products, primarily linear alkanes and alkenes. The main reactions occurring during the F-T process result in the generation of paraffins (Equation (1-1)), olefins (Equation (1-2)) and alcohols (Equation (1-3)), in addition to the water-gas-shift (WGS) reaction (Equation (1-4)).

Paraffins: $nCO + (2n + 1)H_2 \rightarrow C_nH_{2n+2} + H_2O$ (1-1)

Olefins: $nCO + 2nH_2 \rightarrow C_nH_{2n} + nH_2O$ (1-2)

Alcohols: $nCO + 2nH_2 \rightarrow H(-CH_2-)_nOH + (n-1)H_2O$ (1-3)

WGS: $CO + H_2O \leftrightarrow CO_2 + H_2$ (1-4)
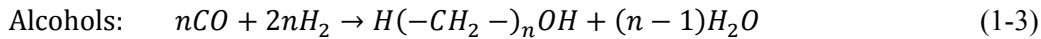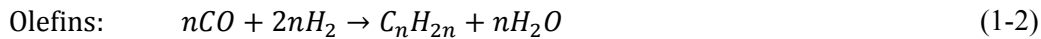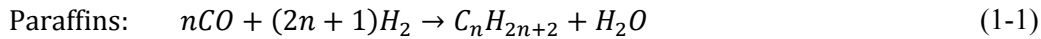
Although many metals have been identified to catalyze F-T reactions, only iron (Fe) and cobalt (Co) have been used in industrial applications. Iron catalyst is cheap and has a high water-gas-shift (WGS) activity, however, it is prone to severe attrition in slurry reactors and the water

produced during the reaction appeared to decrease its activity. Cobalt-based catalyst, on the other hand, has higher activity than iron catalyst since it is not strongly inhibited by water. It is more resistant to attrition and, as such, has a longer life in the reactor than iron catalyst. Cobalt-based catalyst, however, is more expensive than iron catalyst and has no WGS activity. During Cobalt catalyzed F-T reaction, the oxygen from CO dissociation is converted to H_2O. Conversely, iron catalyst has a high affinity for the WGS reaction, resulting in the conversion of a significant portion of oxygen from CO dissociation into CO_2 [20]. Thus, the extent of the WGS reaction has to be closely considered as it affects the H_2/CO ratio in the F-T process.

The F-T synthesis provides a pathway for converting carbon containing natural resources, such as natural gas, coal, heavy residue, biomass, municipal waste, etc., into liquid fuels and high value chemicals in an Anything-to-Liquid (XTL) process, as shown in Figure 2. In this process, the CO and H_2 (syngas) react in the presence of a catalyst, conventionally iron or cobalt, to produce synthetic hydrocarbon products, primarily linear alkanes and alkenes. The overall F-T process involves three main steps: (1) syngas generation, (2) F-T catalytic reactions and (3) product upgrading.
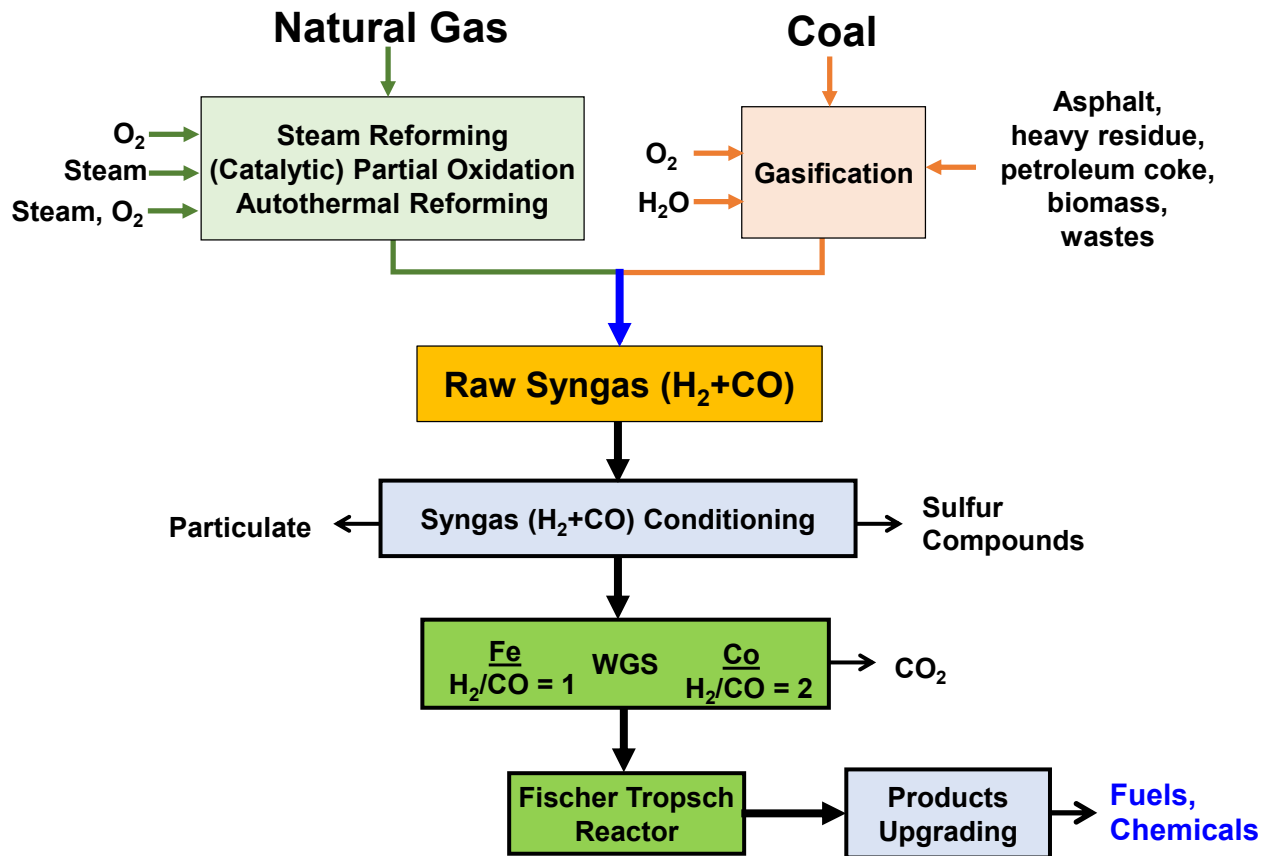
Figure 2: Overview of the Anything-to-Liquid (XTL) process [20]

In the case of gas-to-liquid (GTL) applications, the produced syngas is highly rich in H_2 and any additional H_2 via the WGS reaction is undesirable. In contrast, carbon-rich feedstocks, such as coal or biomass, produce a CO-rich syngas; and would therefore require an extent of WGS in the F-T reactor. Hence, industrial GTL plants have conventionally used cobalt-based catalysts, such as the Shell (Pearl) and the Sasol (Oryx) plants in Qatar, whereas the coal-to-liquid (CTL) plants usually use iron-based catalysts, such as the Sasol Synfuels complex in Secunda, South Africa and the planned CTL plants in China [35-37].

The F-T process configuration could ultimately dictate the type of the catalyst to be used for GTL or CTL applications. For instance, if the process is configured for recycling CO_2 or CO_2-rich tailgas to the methane reformer, this will lower the H_2/CO ratio and will allow the use of iron catalyst in GTL applications. Similarly, if the process is configured for a sour shift of the syngas from the gasifier over Cu/ZnO catalyst, followed by an acid gas (CO_2 and H_2S) removal, this will allow the use of cobalt in CTL applications. Various process configurations for Anything-to-Liquid (XTL) plants can be found elsewhere [37-44].

Depending on the reaction temperature, the F-T process is referred to as low temperature F-T (LTFT) or high temperature F-T (HTFT). The temperature of the LTFT ranges from 180 to 260 °C and the syncrude produced is mainly wax consisting mostly of long chain hydrocarbons, while the temperature of the HTFT process is between 290 and 360 °C and the products are mostly short chain hydrocarbons and gases. Therefore, the final products of the LTFT process consist mostly of diesel, while gasoline production has been the focus of the HTFT [28]. The LTFT syncrude product is easy to upgrade by a hydroprocessing and a fractionation step to obtain naphtha and middle distillate, whereas the HTFT syncrude requires more complex refinery facilities [20, 29, 30]. It should be noted that recent R&D and commercial efforts have been focused on the LTFT due to the current drive for using more diesel engines than gasoline engines, the excellent quality of sulfur-free F-T diesel, and perhaps the mild conditions of the process.

Schematic of different reactors used for F-T process commercial applications are depicted in Figure 3. The circulating fluidized-bed reactor (CFBR) is used for the HTFT process, whereas multi-tubular fixed-bed reactors (FBRs) and slurry-bubble-column reactors (SBCRs) are used for the LTFT process. In addition, microchannel reactors (MCRs) for LTFT process in small-scale

11

applications have been recently receiving increasing attention, even though; no commercial applications are yet available. This study focuses on the MCR technology for F-T synthesis.

In multi-tubular FBRs, the syngas flows through small diameter tubes packed with catalyst at small voidage, resulting in a high pressure drop and an increased operating cost. These reactors have comparatively complex heat transfer characteristics and their maximum production capacity is limited by the amount of heat which can be removed. Hot spots would ultimately result in carbon deposits on the catalyst surfaces and serious plugging of the reactor tubes. These types of reactors, however, have been used to carry out LTFT by both Germany during WWII and Sasol since 1950's as well as by Shell at the Bintulu GTL (Malaysia) and more recently at the Pearl GTL (Qatar) [37, 41, 45-47].

SBCRs, on the other hand, have a simpler design and allow for much higher heat removal efficiencies than multi-tubular FBRs due to the presence of a large volume of the liquid-phase. Its advantages include a much greater flexibility than FBRs and its capital cost is 20 - 40% lower than that of a multitubular FBRs [48]. However, the high mechanical shear on the catalyst resulting in particles attrition and the lack of a reliable system for the fine particles separation from the liquid products, have delayed commercial deployment of SBCRs until the 1990's. Conversely, microchannel reactors have a stationary catalyst bed combined with enhanced heat and mass transfer characteristics. Also, they are typically aimed at exploiting a different market than conventional reactors where their small size is an advantage.

G

Multitubular Fixed Bed:
Gas passes through catalyst
packed tubes
- LTFT: $180-260$ ^{o}C
- $\alpha = 0.70 - 0.75$
- Products: Petrol and chemicals
- Catalysts: Fused Fe, K -promoted

Cooling Water

Catalyst tubes

G

L

L

Slurry Bubble Column:
Bubbles rise through liquid
containing fine suspended solids
- LTFT: $180-260$ ^{o}C
- $\alpha = 0.85 - 0.92$
- Products: Wax, diesel, naphtha
- Catalysts: Supported Co or
  precipitated Fe

Cooling water

G

G

Circulating Fluidized Bed:
Small solid particles suspernded
in upward flowing gas
- HTFT: $320-350$ ^{0}C
- $\alpha = 0.70 - 0.75$
- Products: Petrol and Chemicals
- Catalysts: Fused Fe, K −promoted

Cooling water

Catalyst

G

G

Microchannel Reactor:
Packed channels with highly
active catalyst
- Catalysts: Supported Cobalt
- Cross flow channels for cooling

Catalyst Channels

L

Cooling Water

Figure 3: Typical reactor designs found in the industry for F-T application [20]

2.0   OBJECTIVE

The main objective of this work is to conduct stress analysis calculations and modeling of a microchannel reactor for Fischer-Tropsch synthesis. In order to achieve this objective, the following tasks were performed:

1. A 2-D mechanical reactor model was built in ANSYS workbench 18.2 module to evaluate the physical configuration and required accessories of the MCR.

2. A 3-D structural model was also built in ANSYS to provide fundamental understanding of the von Mises and principle stresses involved in building the MCR.

3. A 2-D model for F-T synthesis in the MCR was developed to investigate the effect of superficial syngas velocity on the CO conversion and temperature distribution in one packed channel of the MCR with (4 mm x 4 mm) cross-sectional area and 150 mm length. The effect of H_2/CO ratios on the CO conversion in one packed channel was also investigated. In addition, effect of H_2/CO ratios on the hydrocarbon yield using a 3600 channels of (4 mm x 4 mm) cross-sectional area and 150 mm length was predicted.

3.0   RESEARCH APPROACH

3.1 MCR STRUCTURE AND MATERIAL PROPERTIES

A schematic of the MCR structure considered in the stress analysis is shown in Figure 4. The MCR is constructed first of Plexiglas and second of 316 Stainless Steel. The properties of the Plexiglas and 316 Stainless Steel are shown in Tables 2 and 3, respectively. Details of stress analysis theory is available elsewhere.
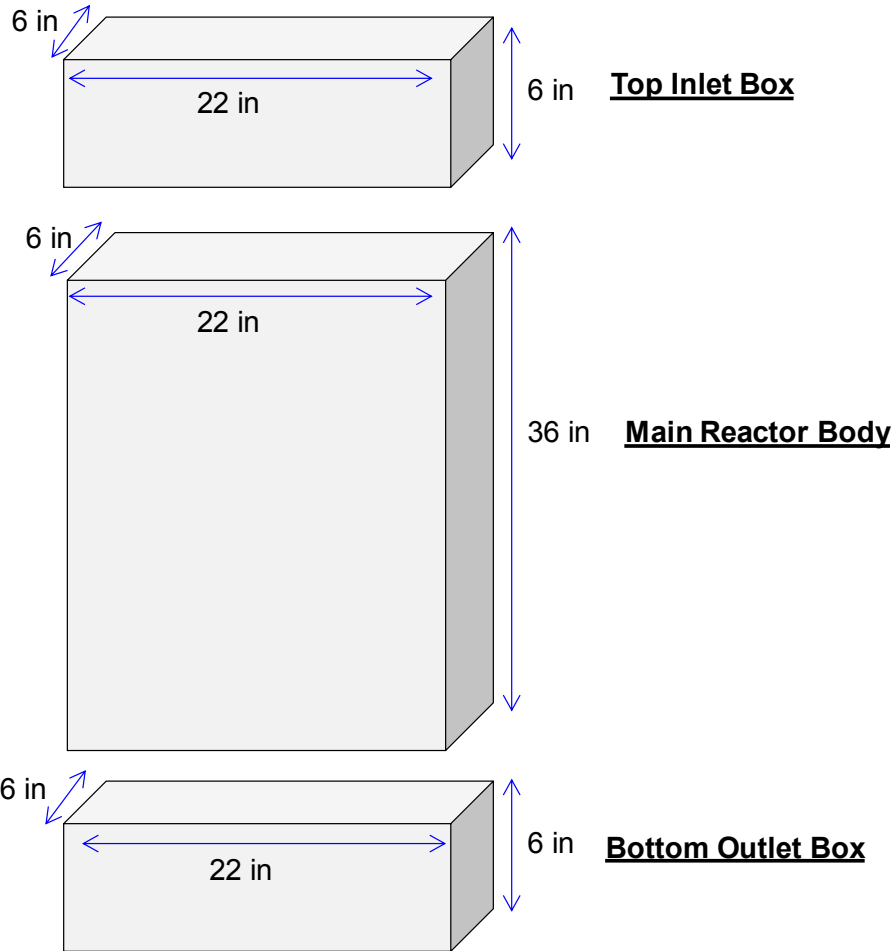
Figure 4: Dimensions and structure of MCR used

Table 2: Properties of Plexiglas [49, 50]

Density (lb/ft³)	86.4
Tensile modulus (psi)	350,000 – 500,000
Tensile Strength (psi)	8,000 – 16,000
Yield Strength (psi), σ_{yp}	12,100
Tensile elongation at Break (%)	2
Compressive strength (psi)	11,000 – 19,000
Plane strain fracture toughness (psi$\sqrt{in}$), K_{Ic}	10
Poisson's Ratio	0.35

Table 3: Properties of 316 Stainless Steel [51]

Density (lb/ft³)	514.9
Modulus of Elasticity (psi)	28,000,000
Plane strain fracture toughness (psi$\sqrt{in}$), K_{Ic}	45,000
Tensile Strength, Ultimate (psi)	84100
Yield Strength (psi), σ_{yp}	217,000
Tensile elongation at Break (%)	50
Compressive strength (psi)	44961.7
Poisson's Ratio	0.27

3.2 2-D STRESS ANALYSIS

A 2-D stress analysis was investigated at the inlet surface of the MCR. It consists of a sheet provided with two holes, one as a gas inlet and the other as a vent, as shown in Figure 5.
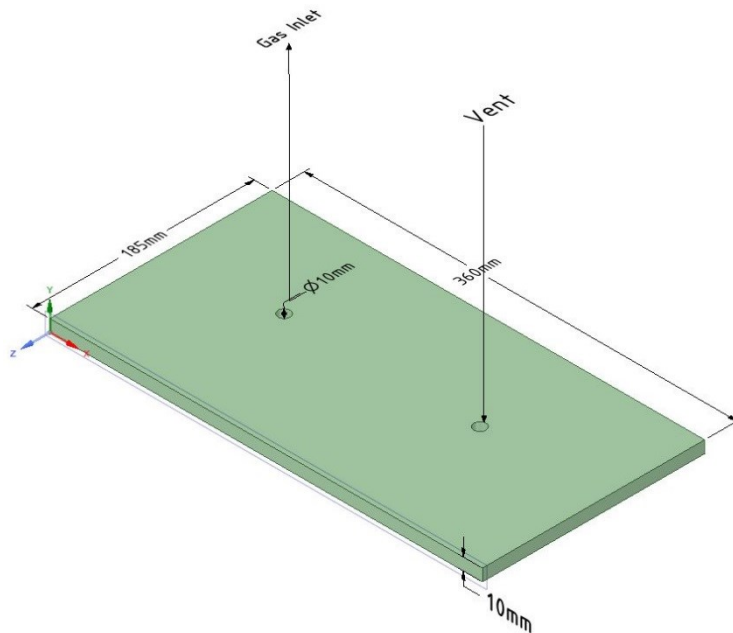
Figure 5: 3-D and 2-D structure of MCR inlet with two holes

Two types of stresses are evaluated for the inlet surface of the MCR, namely Total deformation and von Mises. Total deformation is the deformation caused by the stresses applied on the surface due to displacement. Von Mises stress is related to distortion energy in which a volume element is subjected to principal stresses σ_1, σ_2, and σ_3 where the principal stresses are divided into two parallel components in each direction. One of them, the stress component (S) is equal in all three directions described as a hydrostatic stress component, which changes the volume and contributes to dilatation energy.

Three main types of failure are investigated as follows:

3.2.1   Failure by Yielding

The failure by yielding will occur, if the magnitude of the stress (σ) reaches the critical material strength parameter, which is the uniaxial yield point strength (σ_{yp}). The maximum allowable tensile load P_{y-all}, representing the maximum pressure before which yielding failure occurs, is calculated using Equation (3-1) [52]. A safety factor of 1.5 was recommended.

$$P_{y-all} = \left(\frac{\sigma_{yp}}{n}\right) \cdot A_n \qquad\qquad (3\text{-}1)$$

Where n is the safety design factor, which was taken to be 1.5 in this work.

3.2.2   Failure due to rapid crack extension

The failure due rapid crack extension is determined by assuming the formation of a brittle fracture along a single edge. The maximum allowable load is calculated using Equation (3-2**)**.

$$p_{bf-all} = \left(\frac{\sigma_{bf}}{n}\right) \cdot A_g \tag{3-2}$$

The minimum thickness required (B) for crack propagation is calculated using Equation (3-3**)**.

$$B = 2.5 \left(\frac{K_{Ic}}{\sigma_{yp}}\right)^2 \tag{3-3}$$

Using the information provided in Tables 2 and 3 and Equations (3-1) to (3-3), the minimum thickness was calculated to be 1.76×10^{-6} inch for Plexiglas and 0.107 inch Stainless steel. Therefore, the current thickness of 0.39 inch is sufficient for the potential formation and propagation of a crack.

3.2.3   Failure by brittle fracture

The maximum stress for the formation of a brittle fracture was calculated using Equation (**3-4)** [53].

$$\sigma_{bf} = \frac{K_{Ic}}{C\sqrt{\pi a}} \tag{3-4}$$

Where a represents the crack length and C is a semi-empirical parameter that is derived from stress concentration factor charts, which are available elsewhere [53].

3.2.4 Stress concentration factor near the inlet and vent hole

Failures in structures always initiate at sites of local stress concentrations caused by geometrical discontinuities. These stress concentrations often lead to local stresses many times higher than the nominal net section stress. Therefore, in order to account for the existence of deformities, the actual maximum stress is determined using Equation (3-5).

$$actual\ maximum\ stress = \ K \cdot \sigma_{nom} \qquad \text{(3-5)}$$

Where:

σ_{nom} is the nominal stress, calculated using Equation (3-6).

$$\sigma_{nom} = \frac{P}{A} = \frac{P}{(w - 2r)t} \qquad \text{(3-6)}$$

In the above equation:

K is the stress concentration factor near the holes for gas inlet and vent, which is determined graphically using Figure 6 [53];

r is the radius of the hole (1 cm); and

w is the width of the surface (18.5 cm).
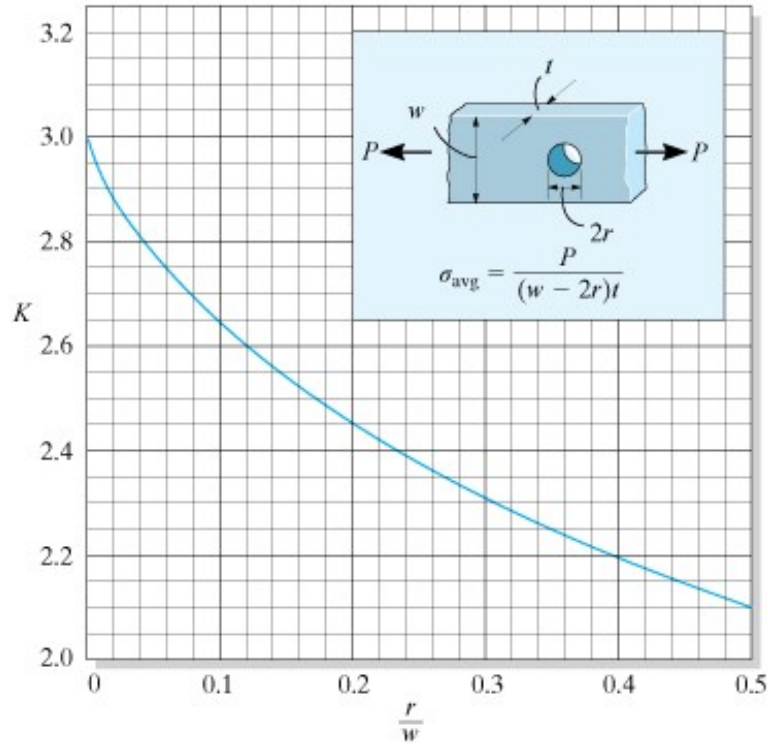
Figure 6: Stress concentration factors for flat MCR inlet with holes (Taken from [53])

3.3 3-D FINITE ELEMENT METHOD FOR STRESS ANALYSIS

ANSYS v 2018 was used to perform Finite Element Method (FEM) Analysis to determine the displacements, normal stresses and principal stresses on the different components of the MCR. A four node quadrilateral element, with two degrees of freedom at each node, was used to compute the two-dimensional FEM analysis on the inlet surface. Also, an eight node brick element with 3 translational degrees of freedom at each node, was used to calculate the 3-D FEM analysis. The equations used in this analysis are given below.

3.3.1 Plane stress formulation on Inlet

The general state of stress at a point is defined by Equation (3-7) as shown in Figure 7:

$$[\sigma]^T = [\sigma_{xx} \quad \sigma_{yy} \quad \sigma_{zz} \quad \tau_{xy} \quad \tau_{yz} \quad \tau_{xz}] \tag{3-7}$$

For a plane stress situation in which there is a unidirectional pressure exerted on the surface, the shear stresses are ignored and the stress reduces to three components as given in Equation (3-8).

$$[\sigma]^T = [\sigma_{xx} \quad \sigma_{yy} \quad \tau_{xy}] \tag{3-8}$$
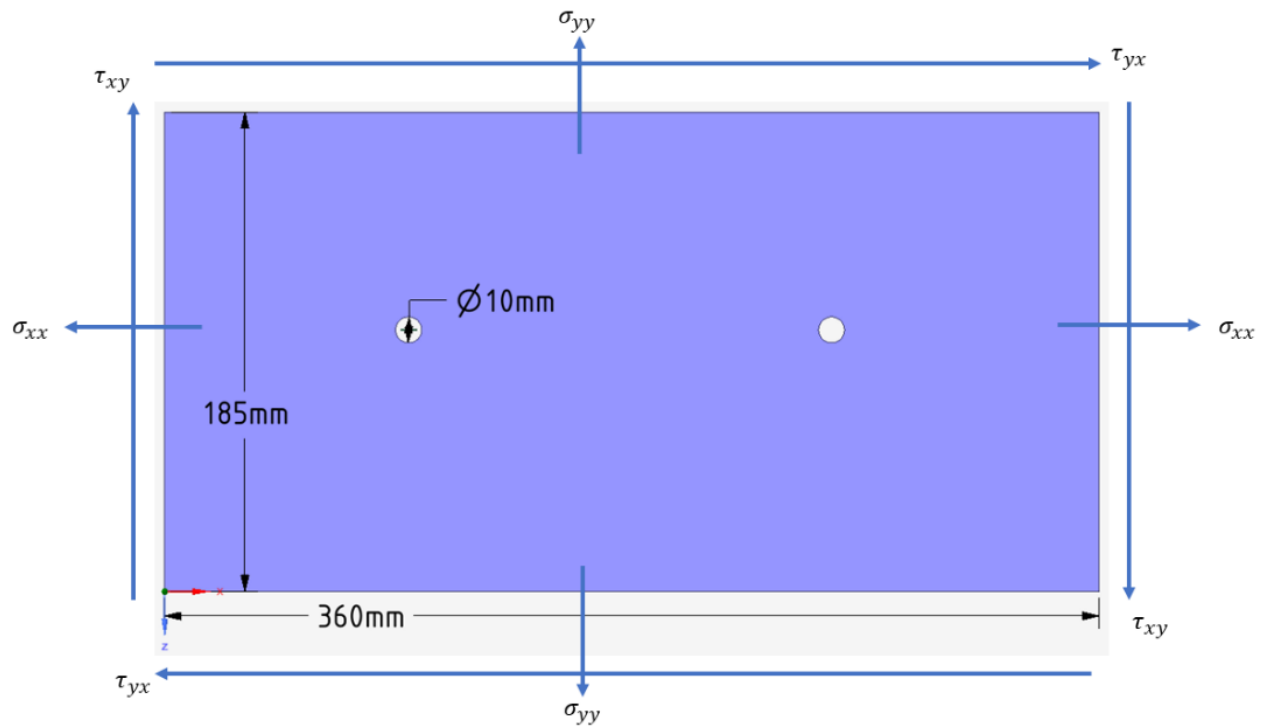
Figure 7: Top view of Inlet surface of MCR

An applied force will create stresses within the structure and cause the body to deform or change its shape. Therefore, a displacement vector is used to account for the changes in the position of any point within the body. A displacement vector $\vec{\delta}$ can be written in terms of its Cartesian components as:

$$\vec{\delta} = u(x, y, z)\vec{i} + v(x, y, z)\vec{j} + w(x, y, z)\vec{k} \qquad (3\text{-}9)$$

Where i, j, and k are the components of the displacement vector representing the difference in the coordinates of the displacement at the point from its original position (x, y, z) to a new position (x', y', z') caused by a loading given by Equations (3-10) through (3-12).

$$u(x, y, z) = x' - x \qquad (3\text{-}10)$$
$$v(x, y, z) = y' - y \qquad (3\text{-}11)$$
$$w = (x, y, z) = z' - z \qquad (3\text{-}12)$$

To better measure the size and shape of the deformations which occur locally within the material, the normal and shear strains are needed. The state of strain at a point is also characterized by six independent components:

$$[\varepsilon]^T = \begin{bmatrix} \varepsilon_{xx} & \varepsilon_{yy} & \varepsilon_{zz} & \gamma_{xy} & \gamma_{yz} & \gamma_{xz} \end{bmatrix} \qquad (3\text{-}13)$$

The relationship between the strain and displacement are shown in Equations (3-16):

$$\varepsilon_{xx} = \frac{du}{dx} \qquad \varepsilon_{yy} = \frac{dv}{dy} \qquad \varepsilon_{zz} = \frac{dw}{dz}$$

$$\gamma_{xy} = \frac{du}{dx} + \frac{dv}{dy} \qquad \gamma_{yz} = \frac{dv}{dz} + \frac{dw}{dy} \qquad \gamma_{xz} = \frac{du}{dz} + \frac{dw}{dx}$$

(3-14)

Over the elastic region of a material, a relationship between the states of stresses and strains exists according to Hook's law [54, 55]:

$$\varepsilon_{xx} = \frac{1}{E} \left[\sigma_{xx} - v(\sigma_{yy} + \sigma_{zz}) \right]$$

$$\varepsilon_{yy} = \frac{1}{E} \left[\sigma_{yy} - v(\sigma_{xx} + \sigma_{zz}) \right]$$

(3-15)

$$\varepsilon_{zz} = \frac{1}{E} \left[\sigma_{zz} - v(\sigma_{xx} + \sigma_{yy}) \right]$$

$$\gamma_{xy} = \frac{1}{G} \tau_{xy} \ ; \quad \gamma_{yz} = \frac{1}{G} \tau_{yz} \ ; \quad \gamma_{zx} = \frac{1}{G} \tau_{zx}$$

Where E is the modulus of elasticity (Young's modulus);

v is the poisons ratio; and

G is the shear modulus of elasticity (modulus of rigidity).

In a plane stress situation, in which no displacements occur in the z direction, Hook's law reduces to:

$$\{\sigma\} = [v]\{\varepsilon\}$$

(3-16)

Where:

$$\{\sigma\} = \begin{bmatrix} \sigma_{xx} \\ \sigma_{yy} \\ \tau_{xy} \end{bmatrix}, \qquad [v] = \frac{E}{1-v^2}\begin{bmatrix} 1 & v & 0 \\ v & 1 & 0 \\ 0 & 0 & \dfrac{1-v}{2} \end{bmatrix}, \qquad [\varepsilon] = \begin{Bmatrix} \epsilon_{xx} \\ \varepsilon_{yy} \\ \gamma_{xy} \end{Bmatrix}$$

For a solid material under biaxial loading, the strain energy $\Lambda^{(e)}$ is

$$\Lambda^{(e)} = \frac{1}{2}\int_v \{\varepsilon^T\}[v]\{\varepsilon\}\, dV \tag{3-17}$$

A Finite Element Formulation of the plane stresses using the Plane 42 element in ANSYS was carried out using the above generalized equations.

3.3.2 3-D FEM Analysis for MCR Components

The eight nodal brick element as shown in Figure 9 was used in the 3-D structural analysis for the MCR body. The geometry of the MCR used in the FEM analysis is shown in Figure 9.
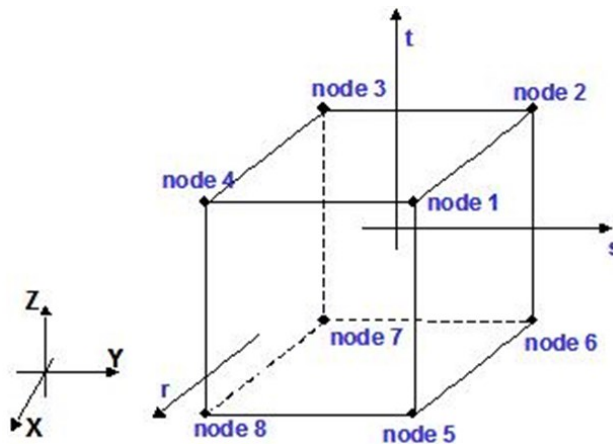
Figure 8: 8 nodal block element used in the FEM analysis
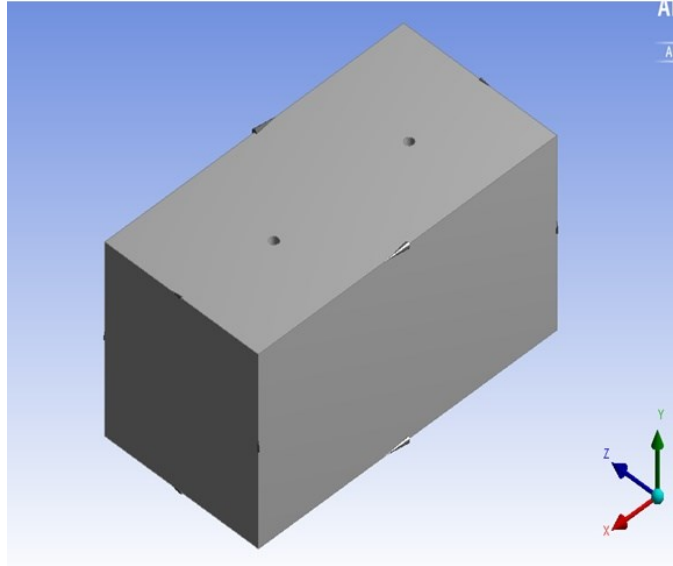
(a)
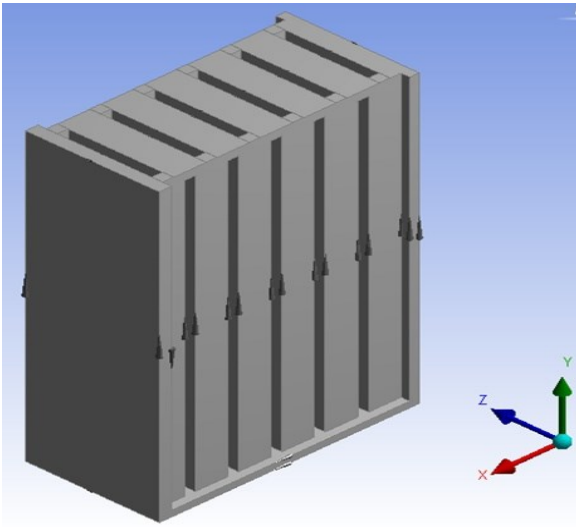
(b)
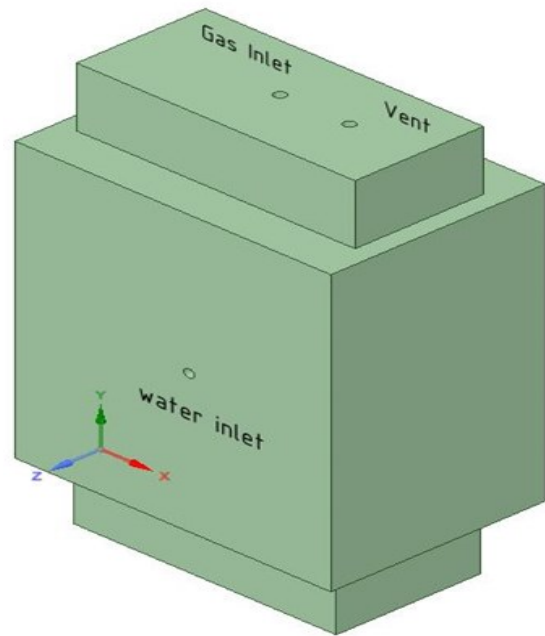
(c)

Figure 9: MCR geometry used in the FEM analysis: (a) MCR inlet, (b) MCR internal channels structure and (c) Overall MCR geometry

The elements displacement field in terms of the nodal displacements and the shape function can be written as:

$$u = \frac{1}{8}\Big(u_i(1-s)(1-t)(1-r) + u_j(1-s)(1-t)(1-r)\Big)$$

$$+ \frac{1}{8}\big(u_k(1-s)(1-t)(1-r) + u_l(1-s)(1-t)(1-r)\big)$$

$$+ \frac{1}{8}\big(u_m(1-s)(1-t)(1-r) + u_n(1-s)(1-t)(1-r)\big)$$

$$+ \frac{1}{8}\Big(u_o(1-s)(1-t)(1-r) + u_p(1-s)(1-t)(1-r)\Big)$$

(3-18)

$$v = \frac{1}{8}\Big(v_i(1-s)(1-t)(1-r) + v_j(1-s)(1-t)(1-r)\Big)$$

$$+ \frac{1}{8}\big(v_k(1-s)(1-t)(1-r) + v_l(1-s)(1-t)(1-r)\big)$$

$$+ \frac{1}{8}\big(v_m(1-s)(1-t)(1-r) + v_n(1-s)(1-t)(1-r)\big)$$

$$+ \frac{1}{8}\Big(v_o(1-s)(1-t)(1-r) + v_p(1-s)(1-t)(1-r)\Big)$$

(3-19)

$$w = \frac{1}{8}\Big(w_i(1-s)(1-t)(1-r) + w_j(1-s)(1-t)(1-r)\Big)$$

$$+ \frac{1}{8}\big(w_k(1-s)(1-t)(1-r) + w_l(1-s)(1-t)(1-r)\big)$$

$$+ \frac{1}{8}\big(w_m(1-s)(1-t)(1-r) + w_n(1-s)(1-t)(1-r)\big)$$

$$+ \frac{1}{8}\Big(w_o(1-s)(1-t)(1-r) + w_p(1-s)(1-t)(1-r)\Big)$$

(3-20)

Where s, t, and r are the shape functions at each node [56].

3.3.3 Simulation Conditions

The following material properties were used by default by ANSYS during the simulation.

Table 4: Plexiglas (PMMA) properties used by ANSYS

Property	Value	Unit
Density	1186	kg/m^3
Young's Modulus	3.1 x 10^9	Pa
Poison's ratio	0.35	
Bulk modulus	3.44 x 10^9	Pa
Shear modulus	1.14 x 10^9	Pa

Table 5: Stainless Steel properties used by ANSYS

Property	Value	Unit
Density	7850	kg/m^3
Young's Modulus	2 x 10^{11}	Pa
Poison's ratio	0.3	
Bulk modulus	1.66 x 10^{11}	Pa
Shear modulus	7.69 x 10^{10}	Pa
Tensile yield strength	2.5 x 10^8	Pa
Comprehensive yield strength	2.5 x 10^8	Pa
Tensile Ultimate Strength	4.6 x 10^8	Pa

3.3.3.1   Inlet surface boundary conditions and applied loads

A fine tetrahedral mesh in a program-controlled element order, as shown in Figure 10, was used to compute the total deformation, and von Mises stresses for hydrostatic pressure load inside the inlet holes, and the pressure load on the inlet rectangular surface of the MCR.

(a)   (b)
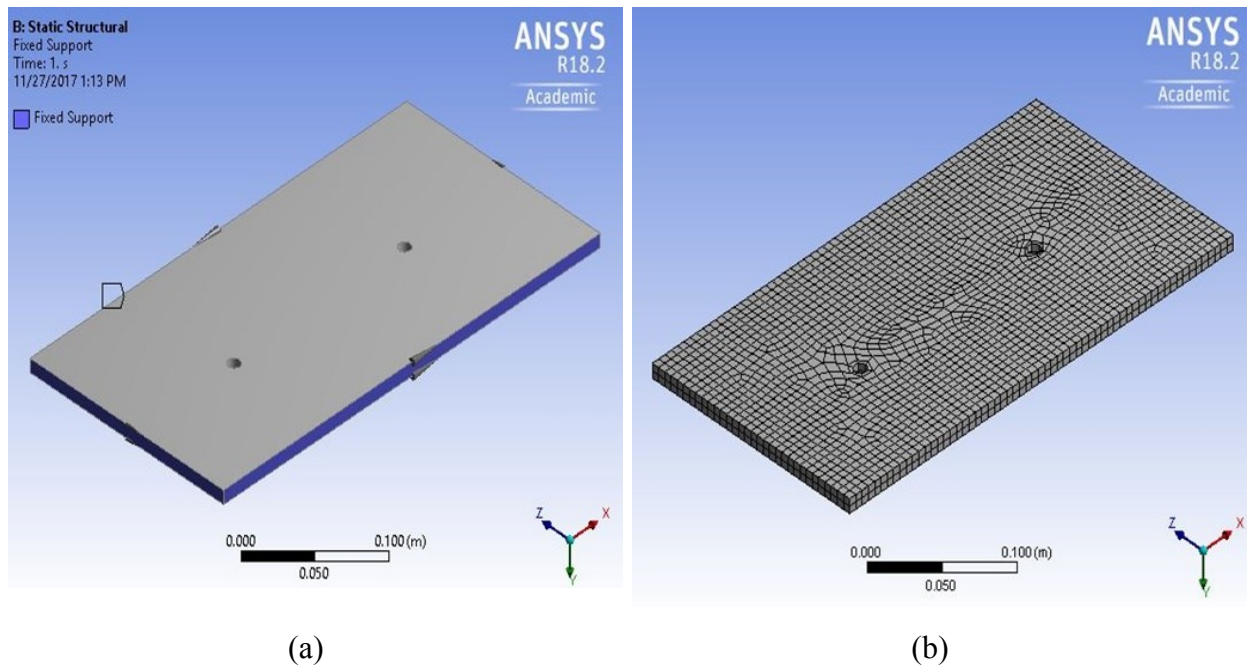
Figure 10: Inlet surface geometry (a) and mesh (b)

The fluid acceleration of $5 \times 10^{-3}\ m/s^2$ was assumed for the flow through the inlet and vent holes and pressure load of $2 \times 10^5\ Pa$ was applied in the upward direction of the surface. After the loads were applied, the ANSYS Mechanical APDL solver solved for total deformation and von Mises stresses using the following formula:

$$U = \sqrt{U_x^2 + U_y^2 + U_z^2} \qquad\qquad (3\text{-}21)$$

$$\sigma_v = \sqrt{1/2[(\sigma_1 - \sigma_2)^2 + (\sigma_2 - \sigma_3)^2 + (\sigma_3 - \sigma_1)^2}} \qquad (3\text{-}22)$$

Where U is the deformed shape and U_i are the component deformations and fixed supports, which prevent deformation. Locations without a fixed support usually experience deformation relative to the original location. The values of von Mises stress are compared to the yield strength of the material to evaluate the design; and the deformation is seen through the contours produced through simulation.

3.3.3.2   Inlet 3-D box boundary conditions and applied loads

Figure 11 shows the dimensions of the inlet box created in ANSYS 18.2. The geometry was modeled using ANSYS static structural to simulate stresses due to internal pressure and forces from inside the reactor.
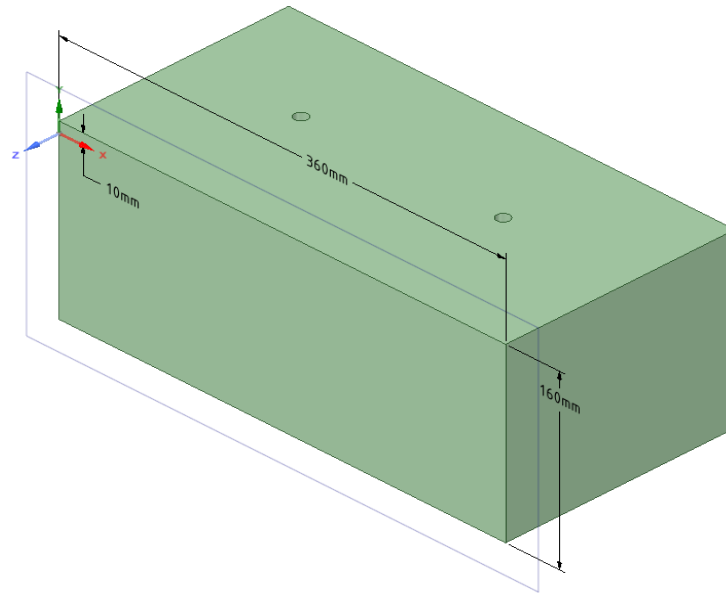
(a)
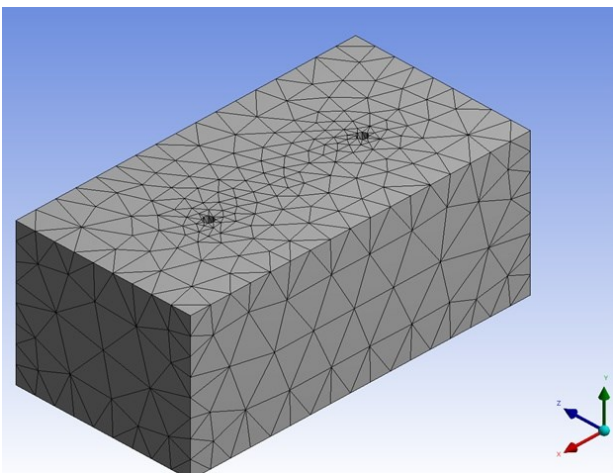
(b)
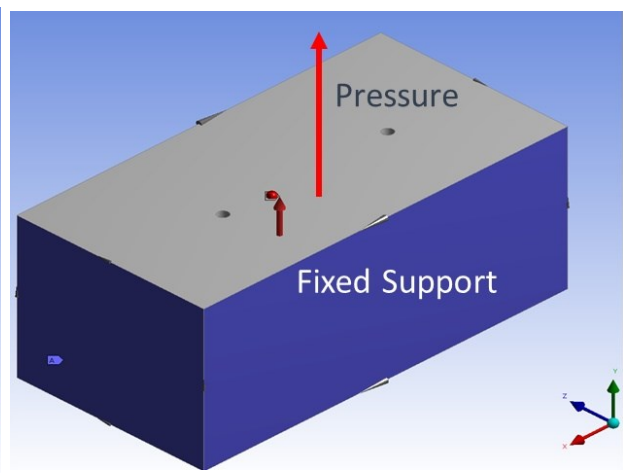
(c)

Figure 11: Inlet enclosure dimensions (a), mesh (b) and boundary conditions(c)

The dimensions of the inlet box structure are 36 cm x 16 cm x 18.5 cm, the inlet box is placed on top of the main body of the MCR. The two holes on the top surface indicate fluid inlet and vent. Each inlet hole is 1 cm in diameter. A stress analysis was performed on this structure to test its structural integrity when subjected to pressure buildup from the inside as well as the high pressure

fluid entering of the MCR. The inlet structure was tested with a pressure of up to 4 atm. inside the reactor. The volume of the inlet box was 2.489 x 10^{-3} m³ and the mass was calculated to be 2.95 kg. There were 4023 nodes detected by the simulation software and 1941 elements. The analysis type was 3-D and was performed with Cartesian type global coordinate system. The mesh used was coarse with bounding box diagonal to be 0.43 m and minimum edge length to be 3.14 cm. The Mechanical APDL solver was used to compute the analysis.

To define loads, four faces were selected for fixed support and one face was selected for pressure load condition. The pressure was applied normal to the inner surface. The maximum magnitude of pressure applied was 4.053 x 10^5 Pa. The analysis was performed to determine the total deformation, equivalent (von Mises) stress, and equivalent elastic strain in the structure. Equations (3-23) and (3-24) were used to compute the total deformation and von Mises stress; and the equivalent (von Mises) elastic strain was computed using Equations (3-23) and (3-24):

$$\sigma_{eq} = E\varepsilon_{eq} \tag{3-23}$$

$$\epsilon_e = \frac{1}{1+v'}\left(\frac{1}{2}[(\varepsilon_1 - \varepsilon_2)^2 + (\varepsilon_2 - \varepsilon_3)^2 + (\varepsilon_3 - \varepsilon_1)^2]\right)^{1/2} \tag{3-24}$$

3.3.3.3   Channels boundary conditions and applied loads

The MCR consists of ten channels, with alternative gas and cooling water flow channels to allow for heat removal. The gases flow from the top to bottom and the cooling water flows horizontally from right to left. To understand the nature of deformation and stresses on the channels, stress analysis was conducted by applying pressure load on the top of the channels and hydrostatic pressure inside the channels.

The geometry of the prototype was built in ANSYS 2018. The dimensions of the MCR are shown in Figure 12. The MCR construction material for this simulation was structural steel, the properties of which are given in Table 9. The volume of this structure is 17,738 cm³ and the mass was calculated by the software to be 139.25 kg. The scale factor value is taken as 1. There are 10,578 nodes and 5,335 elements in this structure. A water of density of 1000 kg.m⁻³ was allowed to flow through all five liquid channels in the horizontal direction as shown in Figure 12 and a hydrostatic acceleration of 10 m/s^2 was assumed. The direction of water flow was also the direction of the hydrostatic pressure. The effect of this fluid pressure allows computing the deformation in the channels. The mesh was created with a coarse element sizing as shown in Figure 12 with a bounding box diagonal of 64 cm and a minimum edge length of 0.051 cm. Two forces were defined, one within the channels, which corresponds to the hydrostatic pressure, and the other on the sides of the reactor, which corresponds to fixed support. A pressure of magnitude 4 atm. was applied on top of the reactor.

The nonlinear effects and thermal strain effects were considered in structural steel material. The moment of inertia was calculated by the solver in the range of 2.07 to 4.7 kg.m^2. The constants listed in Table 6 were used in computing the principal stress and total deformation.
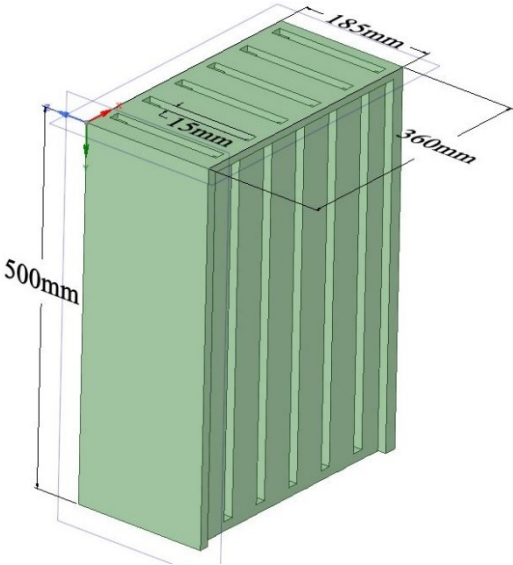
(a)
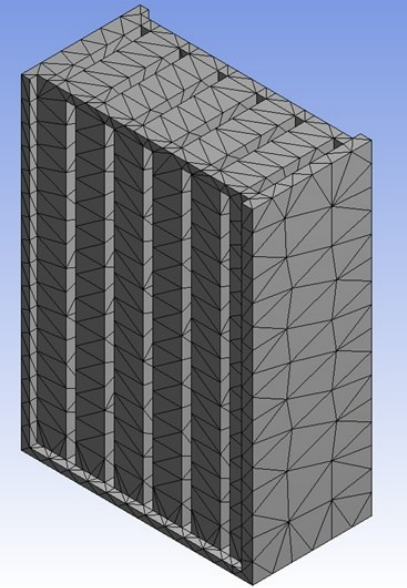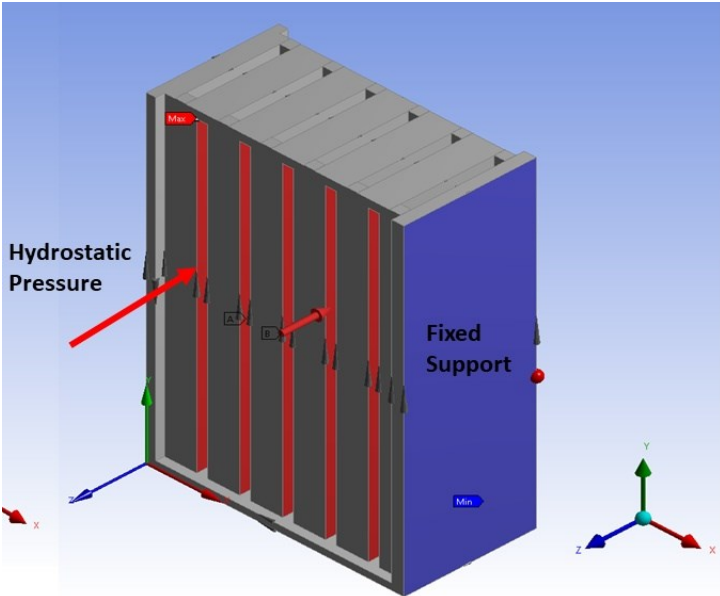
(b)   (c)

Figure 12: MCR channels dimensions (a), mesh (b) and boundary conditions (c)

Table 6: Stress constants for structural steel material

Density (Structural Steel)	7850 kg.m^{-3}
Isotropic secant Coefficient of thermal expansion	1.2 x 10^{-5} C^{-1}
Specific heat constant pressure	434 J $kg^{-1}C^{-1}$
Isotropic thermal conductivity	60.5 W $m^{-1}C^{-1}$
Isotropic resistivity	1.7 x 10^{-7} ohm.m

The principal stresses were calculated by ANSYS using Equation (3-25).

$$\sigma_1 = \sigma_{x'}$$

$$\sigma_2 = \frac{\sigma_{y'} + \sigma_{z'}}{2} + \sqrt{\left(\frac{\sigma_{y'} - \sigma_{z'}}{2}\right)^2} + \sqrt{\tau_{y'z'}^2} \tag{3-25}$$

$$\sigma_3 = \frac{\sigma_{y'} + \sigma_{z'}}{2} - \sqrt{\left(\frac{\sigma_{y'} - \sigma_{z'}}{2}\right)^2} + \sqrt{\tau_{y'z'}^2}$$

3.3.3.4   MCR Boundary Conditions and applied loads

When the inlet surface, top and bottom inlet and outlet boxes and the reactor channels are assembled together, the whole body of MCR is constructed as shown in Figure 13. Unlike the individual reactor parts, the main body was tested for forces and pressures occurring outside the reactor. The main areas of focus are loads due to pipes and accessories and hydraulic pressures at the inlets and outlets of the fluid.

There four openings in total: gas inlet and outlet; water inlet and outlet. Each side is loaded with variable hydrostatic pressure. The density was taken as 1000 kg.m⁻³ for water and 1.165 kg.m⁻³ for nitrogen gas. Each fluid is assumed to have hydrostatic acceleration as 0.5 m/s^2. Along with the hydrostatic pressure, normal pressure of 4 atm. is also loaded at water inlet. The whole body was meshed with triangular coarse meshing and default element size taken by the solver. The number of nodes and elements were 12656 and 6626, respectively. Structural steel material data were used in this simulation.

<div align="center">(a)   (b)</div>
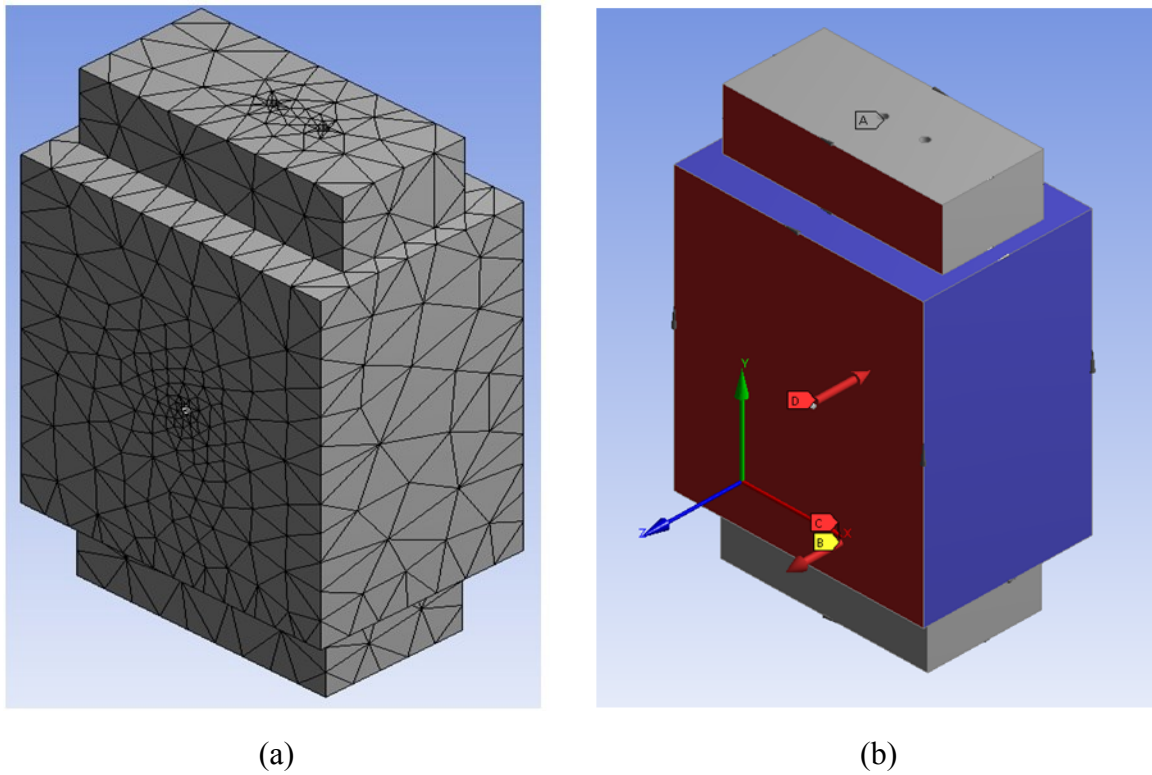
Figure 13: Overall MCR mesh (a) and boundary conditions (b)

The blue region of the MCR indicates that a fixed support boundary condition was placed representing the reactor sides. The hydrostatic pressure was calculated using Equation (3-26):

$$P_{hyd} = \rho g h \tag{3-26}$$

Where ρ = density of water = 1000 kg/m², g = 9.8 m.s⁻² and h = depth of liquid. The height was determined by the solver using the geometry dimensions of the channels.

The von Mises stresses were based upon distortion energy theory in which if the distortion energy of the material exceeds its yield strength, it will fails as per the equation (3-27).

$$\left[\frac{(\sigma_1 - \sigma_2)^2 + (\sigma_2 - \sigma_3)^2 + (\sigma_3 - \sigma_1)^2}{2}\right]^{1/2} \geq \sigma_y \tag{3-27}$$

Where $\sigma_1, \sigma_2, and \sigma_3$ are the principal stresses and σ_y is the yield strength of the material [57]

3.4 DEVELOPMENT OF A 2-D MODEL FOR MODELING MCRS

As discussed by Steynberg [58], two classes of models can be used, namely, pseudo-homogeneous and heterogeneous models. Pseudo-homogeneous models assume thermal and physical equilibrium between the bulk gas-phase and the solid catalyst's surface. Whereas, heterogeneous models include concentration and temperature gradients between the bulk gas-phase and the solid catalyst surface due to inter-particle heat and mass transfer resistances. Both

models can be implemented with varying degrees of complexity, such as axial and radial mixing, and inter-particle gradients. When modelling fixed-bed reactors, the following guidelines are typically used [58] :

1. Inter-particle heat and mass transfer resistances can be neglected, if the catalyst particle diameters are greater than 1 mm such as in commercial fixed bed reactors. This is due to the relatively low volumetric reaction rates induced by the liquid filled pores and large catalyst diameters.

2. Axial mixing is typically ignored when modeling commercial-scale FBRs due to the relatively large catalyst diameters (~ 1 mm), the tube dimensions (1-2 in ID, 6 -12 m high) and superficial gas velocities (> 0.2 m/s), which result in a relatively high Biot numbers large enough to justify the assumption of plug flow.

3. One dimensional models are sufficient for tube diameters less than 1-in, for reactor design purposes.

4. Liquid effects on the reactor hydrodynamics are minor and the pressure drop can be reasonably predicted using a single gas-phase correlation for packed beds. However, liquid effects on inter-particle mass and heat transfer, cannot be ignored.

In this work, a two-dimensional (2-D) model for only gas-phase reactions was developed to model the MCR, the model is based on a convection diffusion reaction equation of the form:

$$\frac{\partial C_i}{\partial t} = D \cdot \nabla^2 C_i - \bar{u}_i \cdot \nabla C + M \tag{3-28}$$

Where M is a reaction source term.

Upon generic expansion:

$$\frac{\partial C_i}{\partial t} = D \cdot \left[\frac{\partial^2 C_x}{\partial x^2} + \frac{\partial^2 C_y}{\partial y^2} + \frac{\partial^2 C_z}{\partial z^2}\right] - \bar{u}_i \cdot \left[\frac{\partial C_x}{\partial x} + \frac{\partial C_y}{\partial y} + \frac{\partial C_z}{\partial z}\right] + r_i \qquad (3\text{-}29)$$

Assuming symmetry along the y-axis, steady-state and an incompressible velocity field, Equation (3-29) is reduced to the two-dimensional mass balance as follows:

$$\left[D_i^{lateral} \frac{\partial^2 C_{i,x}}{\partial x^2} + D_i^{axial} \frac{\partial^2 C_{i,z}}{\partial z^2}\right] - u_z \cdot \frac{\partial C_{i,z}}{\partial z} + \rho_b \eta_i R_i = 0 \qquad (3\text{-}30)$$

Where:

C_i is the molar concentration of component i.

z and x are the axial and lateral distances.

$D_i^{lateral}$ and D_i^{axial} are the effective lateral and axial dispersion coefficient for component i.

ρ_b is the reactor bulk density.

η_i is the catalyst effectiveness for component i.

R_i is the rate of formation or consumption of component i.

The effective lateral dispersion was calculated using the correlation of Delmas and Froment [59] shown below:

$$D_i^{lateral} = 0.1 u_z d_p \left[1 + 19.4 \left(\frac{d_p}{d_h}\right)^2\right] \qquad (3\text{-}31)$$

Todic et al. [60] mentioned that similar correlations for lateral dispersion result in similar values to those predicted using Equation (3-31). It is important to note, that according to Equation (3-31), the value of the lateral dispersion coefficient increases with decreasing channel diameter.

On the other hand, axial dispersion in packed-bed is a significantly more complex parameter. Measurement and correlations of the axial dispersion coefficient in packed-beds at ambient conditions has been extensively studied and reviewed [61-66], however very few studies were conducted at elevated temperatures and pressures. Therefore in this work, the correlation for axial dispersion by Catchpole and Bernig [62], developed for supercritical CO_2 flow in a 10.3 mm tube packed with 0.1 mm particles, was used:

$$\frac{1}{Pe} = \frac{0.018}{Re} + \frac{10}{\left(1 + \frac{0.7}{Re}\right)}$$

(3-32)

Where:

$$Pe = \frac{d_p u_z}{D_i^{axial}}$$

$$Re = \frac{d_p u_z \rho_i}{\mu_i}$$

The kinetics by Anderson [67] were used to determine the CO consumption rate (Equations (3-33) and (3-34)) and a 2-α probability distribution model ((3-35) to (3-37)) was used to describe the products distribution. The vales for α_1 and α_2 were taken to be 0.659 and 0.941, respectively, as calculated by Arias Pinto [68].

$$(-R_{CO}) \left(\frac{mol}{kg_{cat} \cdot s}\right) = k_{FT} \left(\frac{P_{CO} P_{H2}}{P_{CO} + b P_{H2O}}\right)$$

(3-33)

$$k_{FT} \left(\frac{mol}{kg_{cat} \cdot Pa \cdot s}\right) = 185.97 \exp\left(-\frac{79,900}{RT}\right)$$

(3-34)

$$ln\left(M_f\right) = Ln[A\alpha_1^{n-1} + B\alpha_2^{n-1}]$$

(3-35)

$$B = A\left(\frac{\alpha_1}{\alpha_2}\right)^{\zeta-1} \tag{3-36}$$

$$A = \frac{1}{\frac{1}{1-\alpha_1} + \left(\frac{\alpha_1}{\alpha_2}\right)^{\zeta-1}\left[\frac{1}{1-\alpha_2}\right]} \tag{3-37}$$

Due to the small particle diameters used in MCRs (< 0.2 mm), there are no mass transfer limitations, as previously discussed in the literature [68, 69]. However, pore diffusion limitations were accounted by using the effectiveness factor as shown in Equations (3-38) to (3-40).

$$\eta = \frac{\tanh(\emptyset)}{\emptyset} \tag{3-38}$$

$$\emptyset = l\sqrt{\frac{S_g \rho_{cat}}{\varepsilon_B} \frac{k_R{}'}{D_{i,eff}}} \tag{3-39}$$

$$D_{i,eff} = \frac{\varepsilon_B D_i}{\tau} \tag{3-40}$$

The catalyst specific surface area (Sg) was taken to be 184 m^2/g [70]. The tortuosity value was assumed to be 0.1 [71] and the packed-bed porosity ε_B was 0.3 [68]. The properties of a cobalt catalyst supported on silicon-carbon (70/30 SiC-Co) [71] was used. The catalyst has a particle diameter of 100 μm and a density of 950 kg/m^3. The Peng-Robinson Equation-of-State (P-R EOS), Equation (3-41) was used to obtain the compressibility factor (Z) of the gas mixture.

$$Z^3 - (1 - B)Z^2 + (A - 3B^2 - 2B)Z - (AB - B^2 - B^3) = 0 \tag{3-41}$$

Where:

$$A = \frac{aP}{R^2 T^2} \tag{3-42}$$

$$B = \frac{bP}{RT} \tag{3-43}$$

$$z = \frac{Pv}{RT} \tag{3-44}$$

$$a = \sum_i \sum_j y_i y_j a_{ij} \tag{3-45}$$

$$b = \sum_i y_i b_i \tag{3-46}$$

$$a_{ij} = (1 - \delta_{ij}) \sqrt{a_i a_j} \tag{3-47}$$

$$a_i = 0.45724 \frac{R^2 T_c^2}{P_c^2} \left[1 + \kappa [1 - T_R^{0.5}] \right] \tag{3-48}$$

$$b_i = 0.0778 \frac{RT_c}{P_c} \tag{3-49}$$

$$\kappa = 0.37464 + 1.5422\omega - 0.26992\omega^2 \tag{3-50}$$

The values for the binary iteration parameters were taken from ASPEN Plus.

Similar to the work by Arias Pinto [68], the pressure drop was calculated using the correlation by Eisfeld and Schnitzlein [65], as shown in Equation (3-51).

$$\frac{dP}{dL} = \frac{K_1(1-\varepsilon_B)^2}{d_p^2(\varepsilon_B{}^3)} \left(1 + \frac{2/3}{\left(\frac{d_h}{d_p}\right)(1-\varepsilon_B)}\right)^2 \cdot \mu u$$

$$+ \frac{2(1-\varepsilon_B)}{d_p\varepsilon^3} \frac{1 + \dfrac{2}{3\left(\frac{d_h}{d_p}\right)(1-\varepsilon_B)}}{\left(\left(k_1\left(\frac{d_p}{d_h}\right)^2 + k_2\right)^2\right)} \cdot \frac{\rho u^2}{2} \tag{3-51}$$

Similar to the derivation of the mass balance (Equation (3-28)), the heat balance was derived as follows:

$$\left[\lambda_i^{lateral}\frac{\partial^2 T_{i,x}}{\partial x^2} + \lambda_i^{axial}\frac{\partial^2 T_{i,z}}{\partial z^2}\right] - u_z\rho_g C_p \frac{\partial T_{i,z}}{\partial z} + \rho_b\eta_{CO}(-R_{CO})(-\Delta H_r) = 0 \tag{3-52}$$

Where

ρ_g is the gas phase density.

λ_i^{axial} and $\lambda_i^{lateral}$ are the effective axial and lateral thermal conductivities.

C_p is the gas phase heat capacity.

The boundary conditions required to solve the above system of equations are:

$C_i = C_{i,inlet}$ $\qquad\qquad$ $z = 0 \ and \ 0 \le x \le w$

$u_z = u_{z,inlet}$ $\qquad\qquad$ $z = 0 \ and \ 0 \le x \le w$

$T = T_{inlet}$ $\qquad\qquad$ $z = 0 \ and \ 0 \le x \le w$

$$P = P_{in} \qquad\qquad z = 0 \text{ and } 0 \le x \le w$$

$$\frac{\partial(u_z C_i)}{\partial x} = 0 \qquad\qquad x = 0, x = w, \text{ and } 0 \le z \le l$$

$$\frac{\partial T}{\partial x} = 0 \qquad\qquad x = 0, \text{ and } 0 \le z \le l$$

$$\lambda_i^{lateral} \frac{\partial T}{\partial x} = -h_{wall}(T - T_{wall}) \qquad x = w, \text{ and } 0 \le z \le l$$

The above system of equations was implemented into MATLAB v 2017b, and solved using the solvepde function for a 2-D rectangular geometry. The simulation parameters are summarized in Table 7.

Table 7. Model parameters for F-T calculations in the MCR

Temperature (°C)	K	483
Pressure (bar)	P	25
H₂/CO in the feed gas	-	$1.5 - 2.5$
Inlet gas velocity (m/s)	u	$0.01 - 0.15$
Channel area (mm²)	a_t	4x4
Packed bed length (mm)	L	150
Catalyst particle size (microns)	d_p	100
Bed Porosity	ε_B	0.3
Catalyst density (kg/m³)	ρ_{cat}	4840

4.0   RESULTS AND DISCUSSION

4.1 RESULTS OF 2-D STRESS ANALYSIS

4.1.1   Results of elastic plastic fracture mechanics of the inlet of the MCR

Table 8 shows the calculated maximum allowable loads which the MCR can withstand when constructed with either Plexiglas or structural steel with a thickness of 0.39 inch.

Table 8: Results for elastic plastic fracture mechanics of inlet plate

MCR inlet plate material	Failure by yielding	Failure due to rapid crack extension
Plexiglas	Max. allowable load: 17,035 lb	Max Allowable load: 15 lb
Structural steel	Max. allowable load: 410,737 lb	Max Allowable load: 67,000 lb

4.1.2 Results of stress concentration factor and nominal stress near the inlet and vent holes

Using the K-chart (Figure 6), the values of the stress concentration factor and the nominal stress near the inlet and vent holes were obtained and listed in Table 9.

Table 9: Results of stress concentration near the holes

K	σ_{nom}	σ_{Max}
2.85	2191996 Pa/m²	6247188 Pa/m²

4.2 RESULTS OF 3-D STRESS ANALYSIS

4.2.1   Stress contours on inlet surface for Plexiglas

Figure 14 shows the simulation results of the stress analysis carried out on the inlet surface of the MCR. As can be seen in this figure, the maximum deformation existed at the inlet and vent holes with a value of 9.2×10^{-7} m.

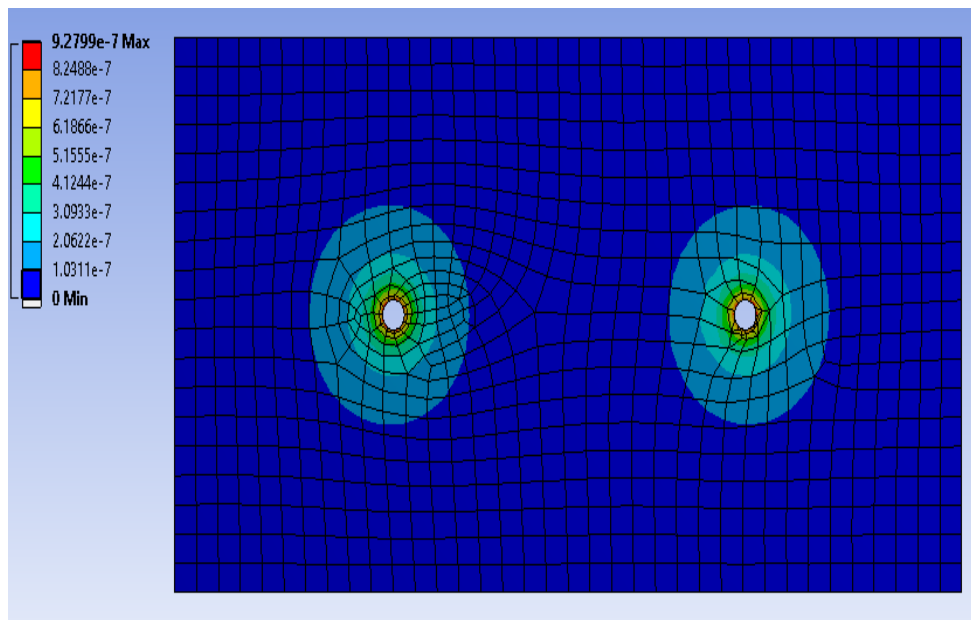**Figure 14: Contours for total deformation on the inlet surface (Plexiglas)**

Figure 15 shows the stress values on the inlet surface, and as can be seen the maximum stress is 4.2×10^7 Pa, whereas the minimum stress is 25,556 Pa, which corresponds to 6,120 and 3.70 psi, respectively. It is important to note that the maximum stress exhibited is lower than the yield strength of the steel.
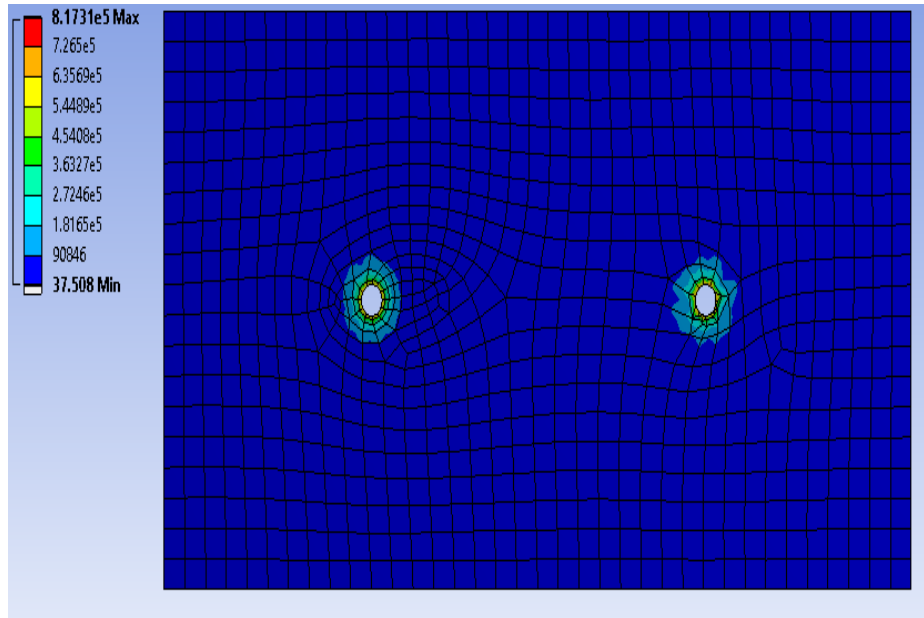
Figure 15: Contours for von Mises stress on the inlet surface (Plexiglas)

4.2.2 Stress contours on the inlet box with vent (Plexiglas)

Figure 16 shows simulation results of the stress analysis conducted on an inlet enclosure box of the MCR at a pressure of 4 atm. Similar to results at the surface, the maximum deformation existed at the inlet and vent holes with a value of 2.6×10^{-3} m, which is represented by the red color on the surface of the structure. The maximum deformation value was significantly higher than that exhibited by the inlet surface, shown in Figure 14. This behavior is primarily due to the existence of fixed walls at the sides of the box which directed and concentrated stress near the holes.

Figure 17 shows the stress values on the inlet surface; and as can be observed the maximum stress is 3.8×10^7 Pa, whereas the minimum stress is 14.58 Pa, which corresponds to 5,511 and 0.002 psi, respectively. Also, the major stress regions in the same figure can be seen near the edges and at the center of the inlet surface, however, these values do not exceed the yield strength of the Plexiglas.
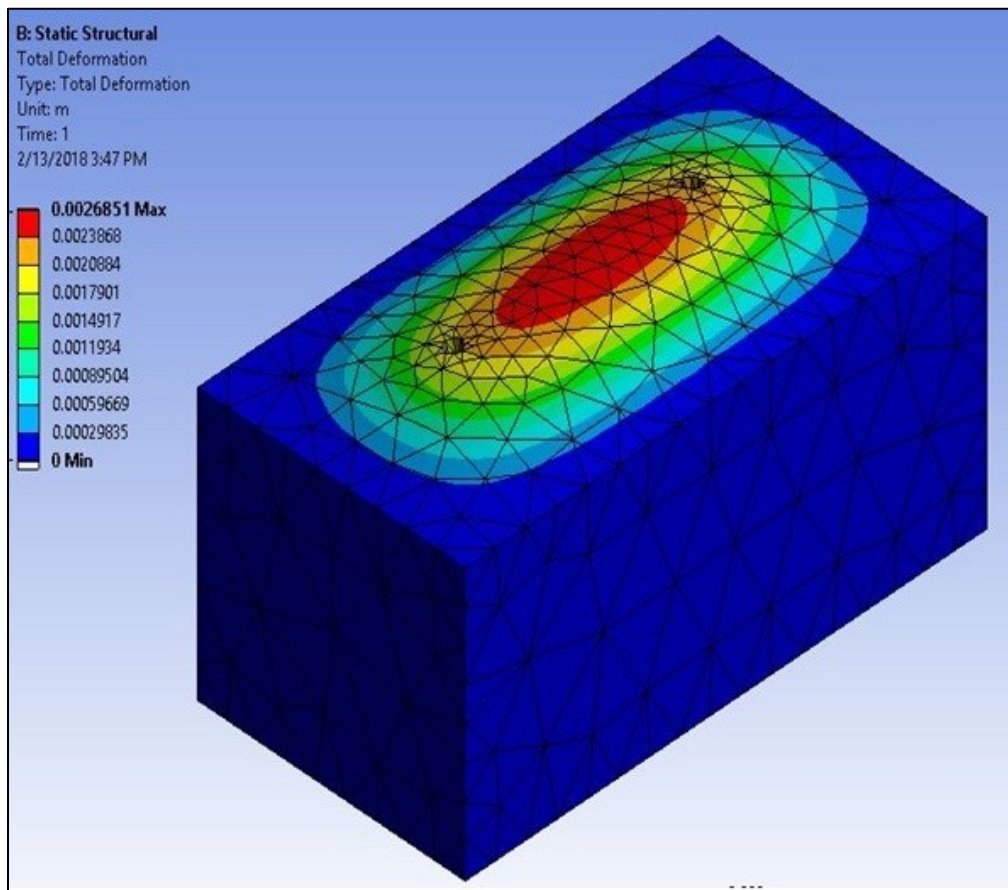
Figure 16: Contours of the total deformation on the inlet box (Plexiglas)
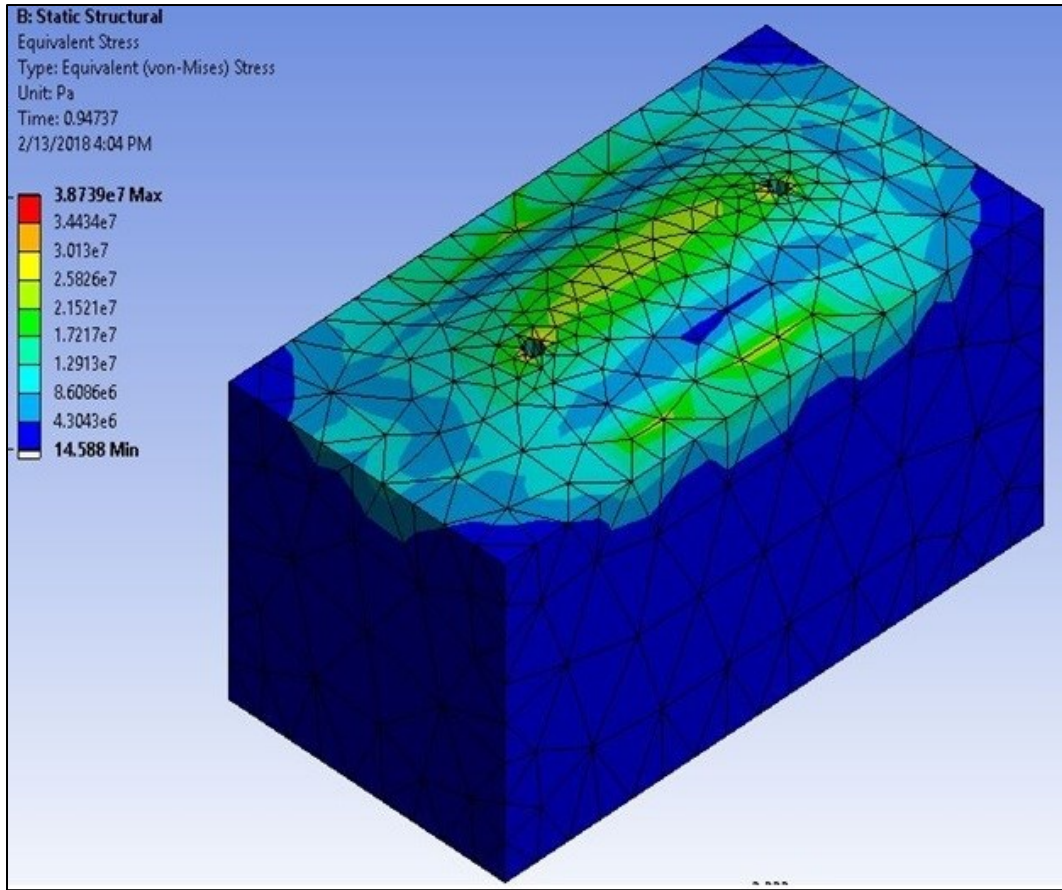
Figure 17: Contours of von Mises stress on the inlet box

4.2.3 Stress contours on the channels of the reactor

Figure 18 shows the simulation results of the stress analysis conducted on a Plexiglas inlet enclosure box of the reactor at a pressure of 4 atm. Similar to results at the surface, the maximum deformation due to applied pressure exists at the top center of the structure with a value of 9.65×10^{-6} m, which is represented by the red color on the surface of the structure. Also, the total deformation exhibited decreases laterally from the center.

In addition, Figure 19 shows the simulation results of von Mises stress analysis due to both mechanical pressure exerted at the top of the structure and the hydrostatic pressure exerted form within the structure due to internal pressurization. As can be seen in this figure, the values of the minimum and maximum von Mises stresses created on the channels are 2,040.9 Pa and 7.26 x 10^6 Pa. It should be mentioned that both these values are under the limit of the yield strength of both Plexiglas and structural steel. On the other hand, the maximum and minimum values of von Mises stress produced due to the hydrostatic pressure within the channels are 4.45×10^{-6} Pa and 2.49×10^9 respectively.
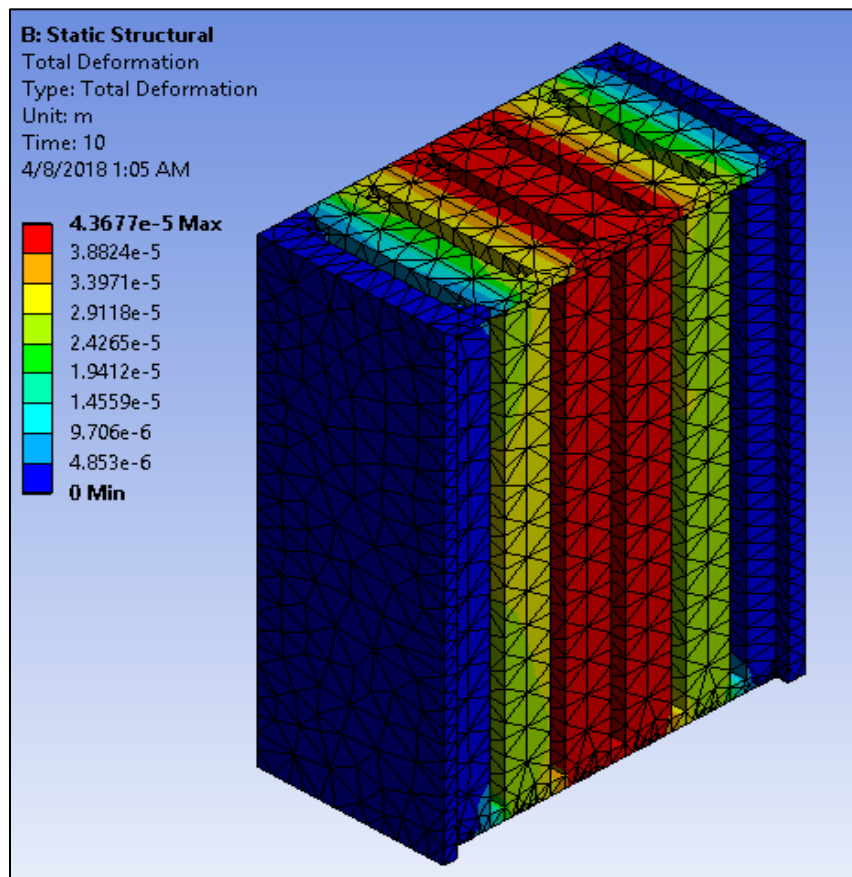
Figure 18: Contours for total deformation on the MCR channels (Plexiglas)
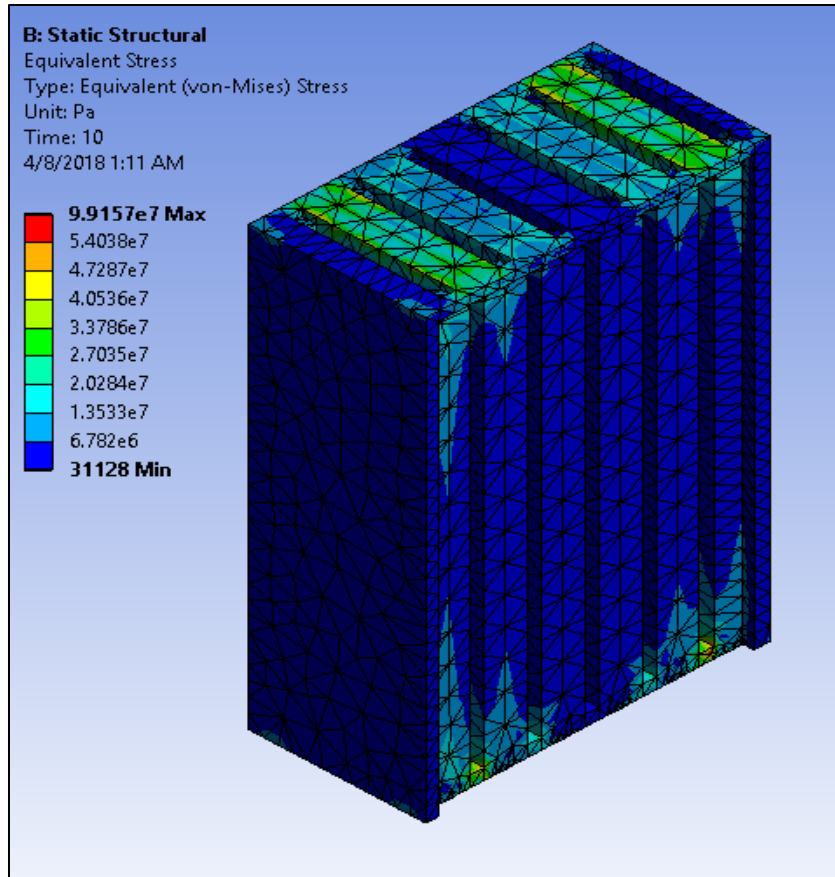
Figure 19: Contours for von Mises stress on the MCR channels

4.3 2-D REACTOR MODEL RESULTS

4.3.1 Effect of inlet velocity on CO conversion

Since a square cross-sectional channel (4 mm x 4 mm) with a 150 mm length is used in the simulations, it is important to note that the Z axis goes through the center of the square and as such there is a symmetry with respect to the X and Y axes. Figures 20 through 24 show the 2-D model predictions of CO conversion contours along the packed channel. As can be seen in these figures,

increasing the gas velocity significantly decreases the conversion along the packed channel length, which is expected. Moreover, CO conversion is always greater near the centerline of the packed channel and decreases laterally in the X and Y directions.

Figure 20: Contours for CO conversion along the packed channel at u = 0.01 m/s H$_2$/CO = 2

Figure 21: Contours for CO conversion along the packed channel at u = 0.025 m/s H$_2$/CO = 2

Figure 22: Contours for CO conversion along the packed channel at u = 0.05 m/s H₂/CO =2
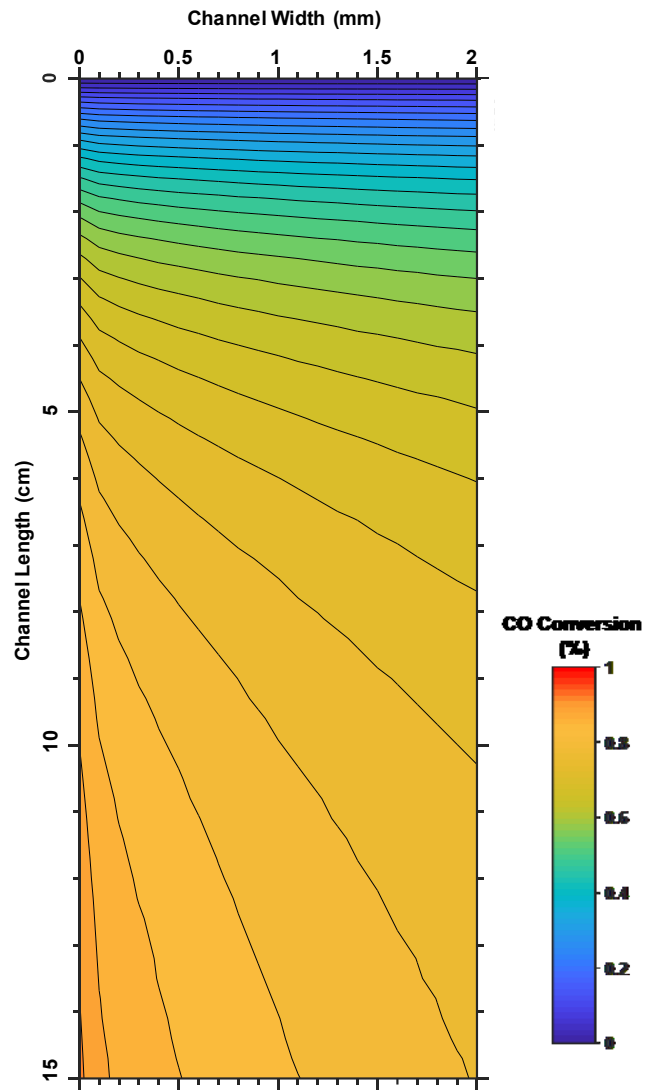
Figure 23: Contours for CO conversion along the packed channel at u = 0.075 m/s H₂/CO =2
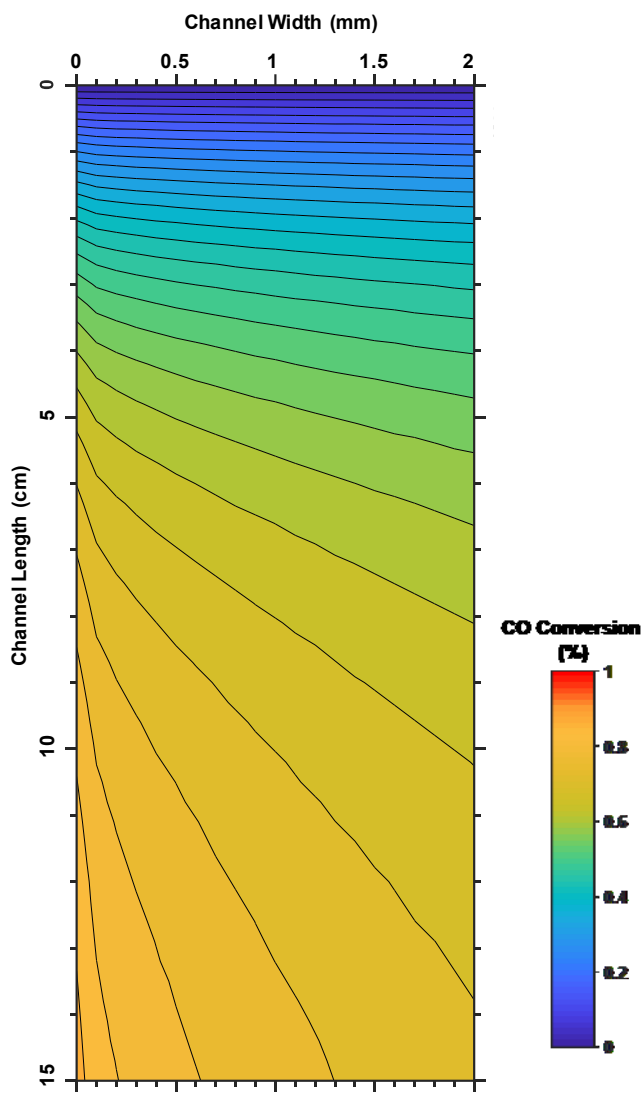
Figure 24: Contours for CO conversion along the packed channel at u = 0.1 m/s H$_2$/CO =2
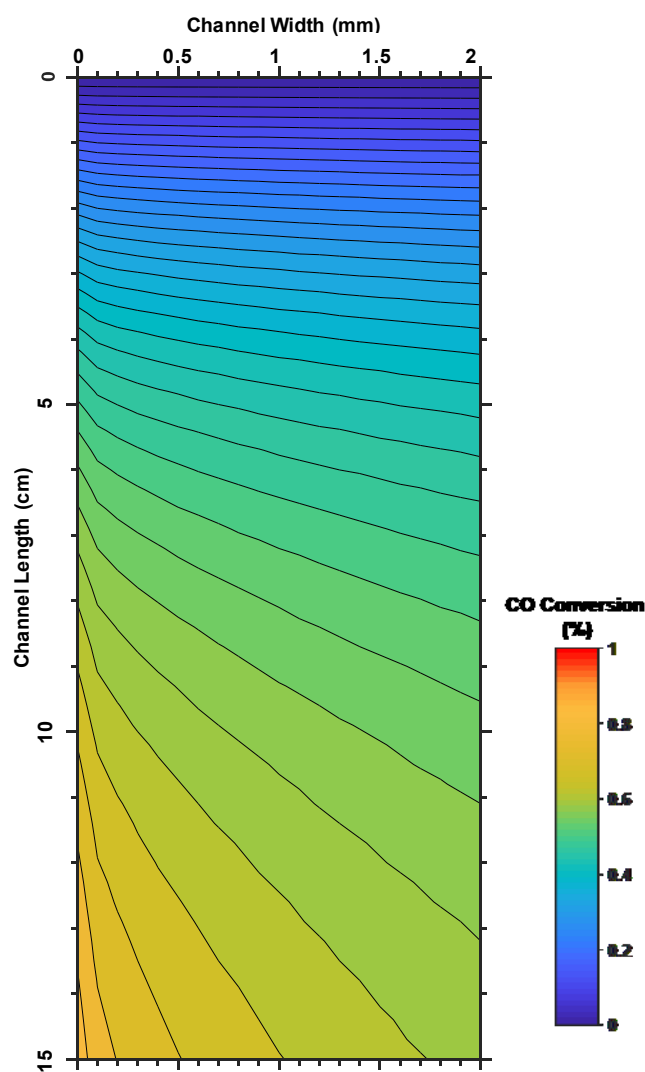
Figure 25: Contours for CO conversion along the packed channel at u = 0.15 m/s H$_2$/CO =2

4.3.2 Effect of inlet velocity on Temperature

Figures 25 through 28 show the 2-D model predictions of the effect of increasing the superficial gas velocity on the temperature contours along the packed channel. As can be observed in these figures, the temperature gradient in the packed channel appears to decrease with increasing the

superficial gas velocity. This behavior is primarily due to lower conversions at higher velocities. Moreover, the highest temperature is always exhibited at the centerline of the packed channel, and the temperature profiles decreases near the outlet, which could be due to the formation of heavier hydrocarbon products with higher heat capacities.
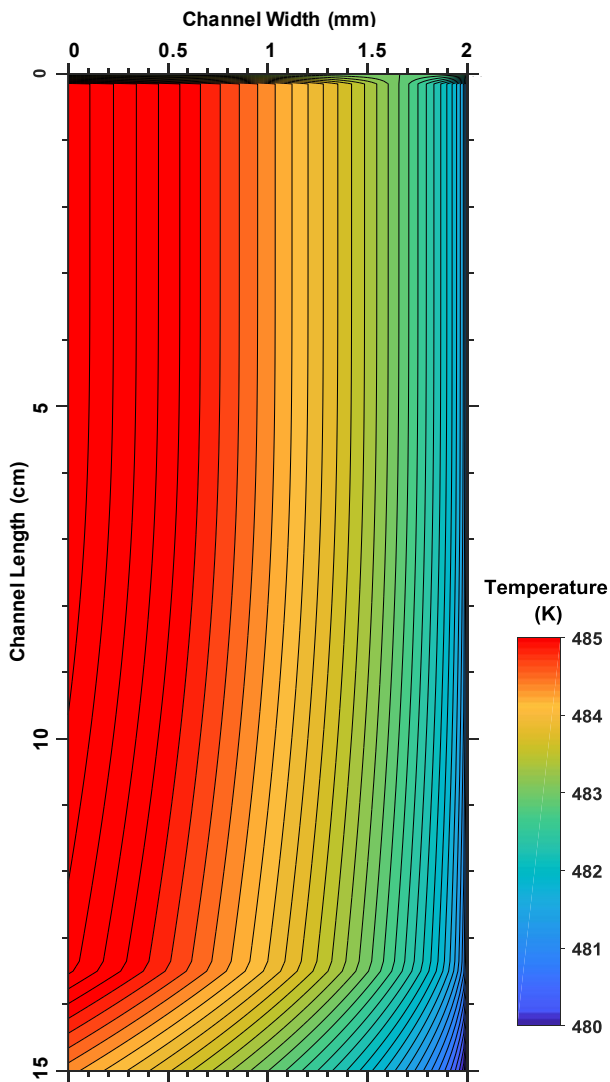
Figure 25: Contours for temperature along the packed channel at u = 0.01 m/s

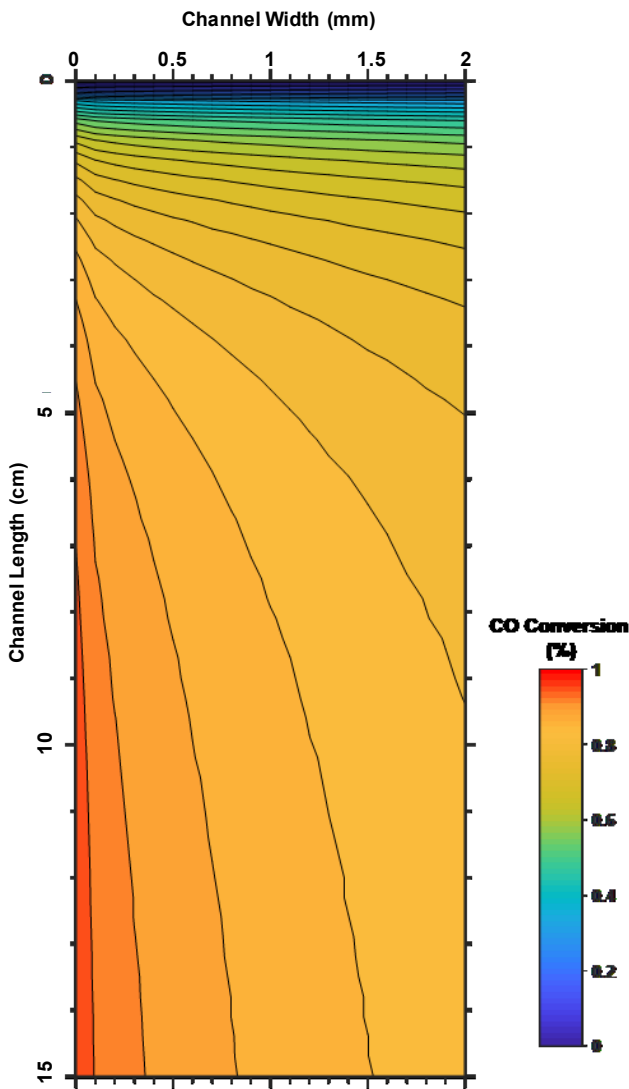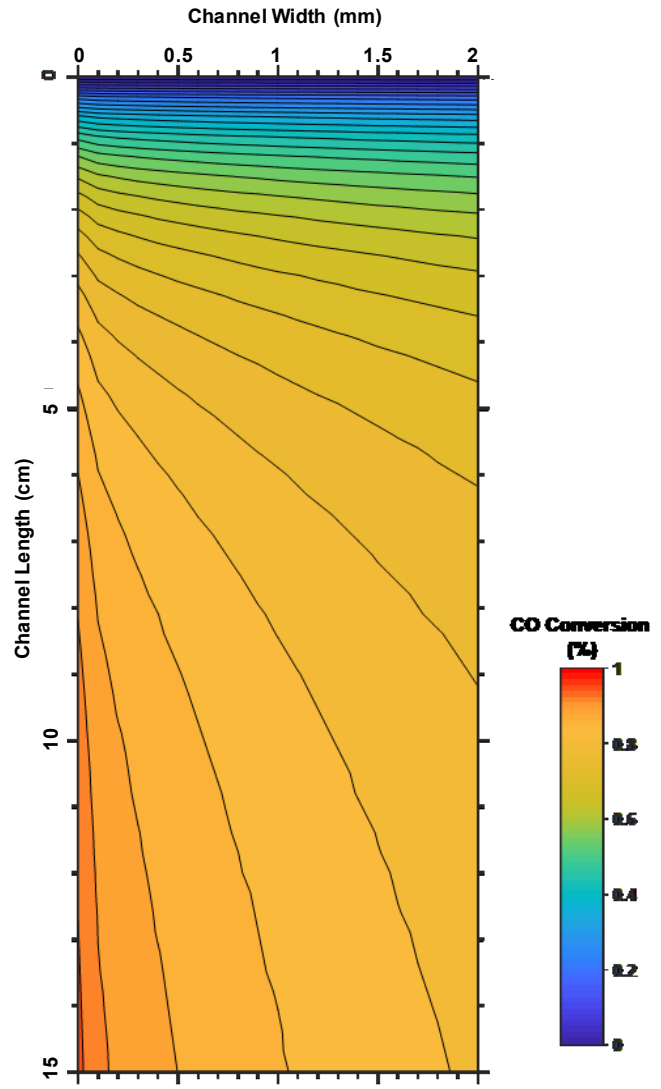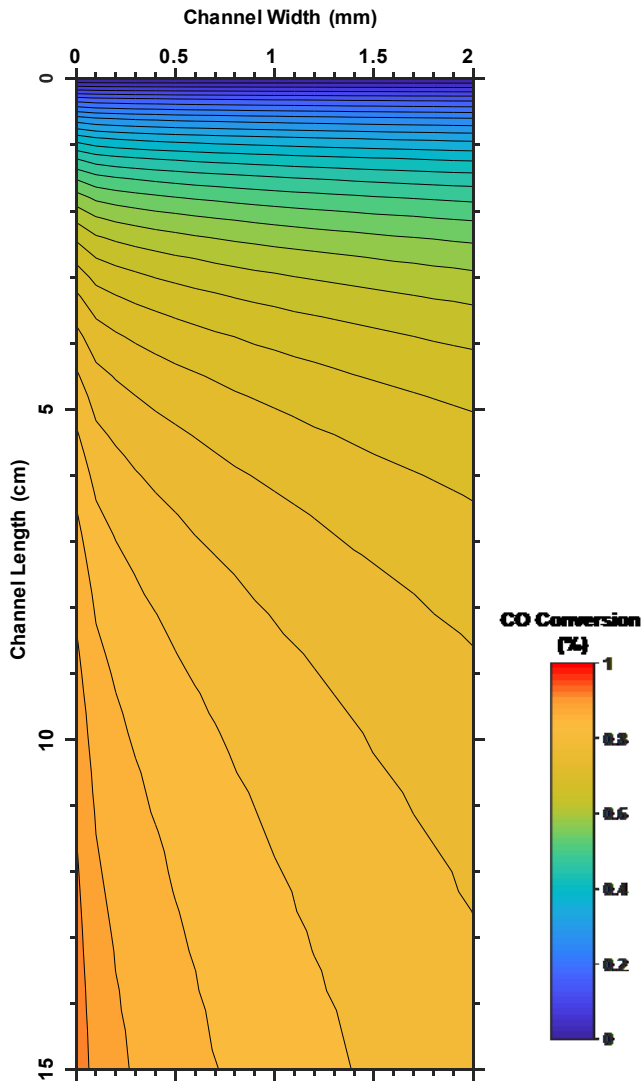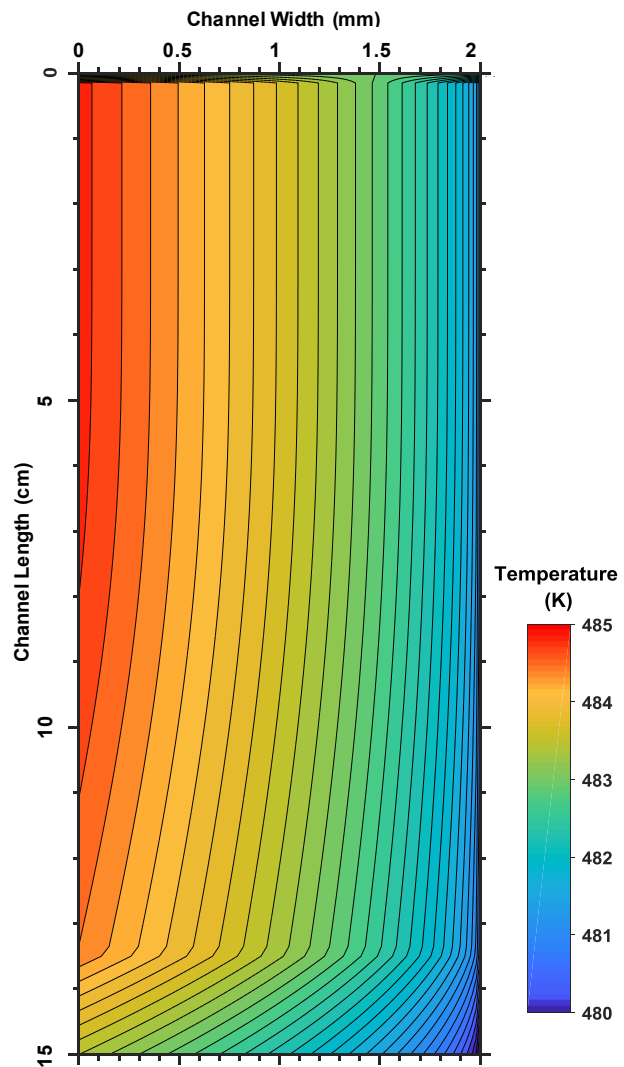**Figure 26: Contours for temperature along the packed channel at u = 0.05 m/s**
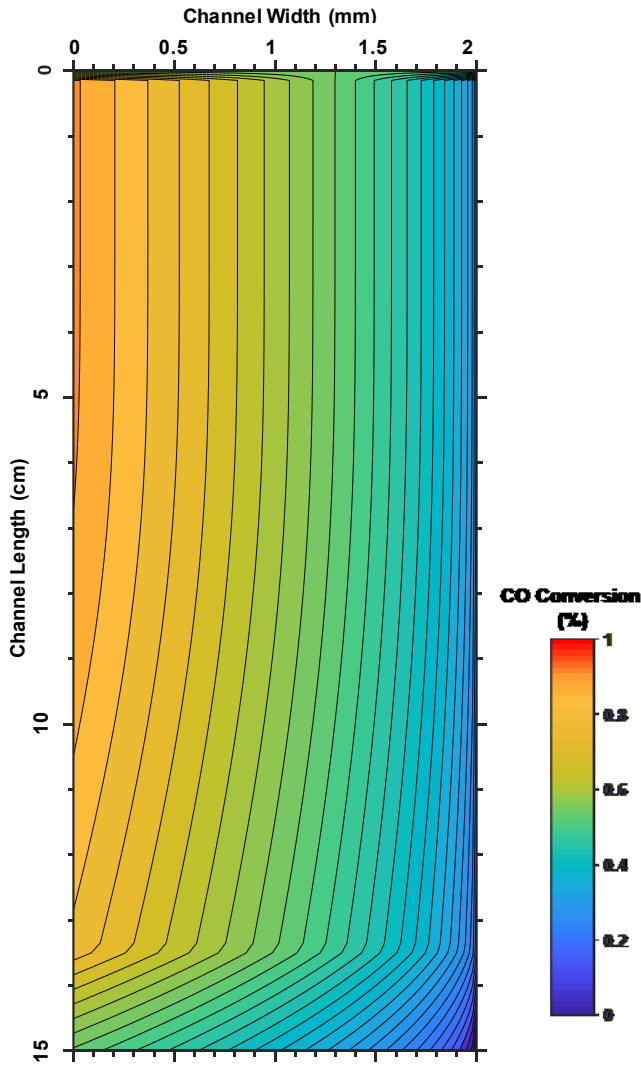
Figure 27: Contours for CO conversion along the packed channel at u = 0.1 m/s
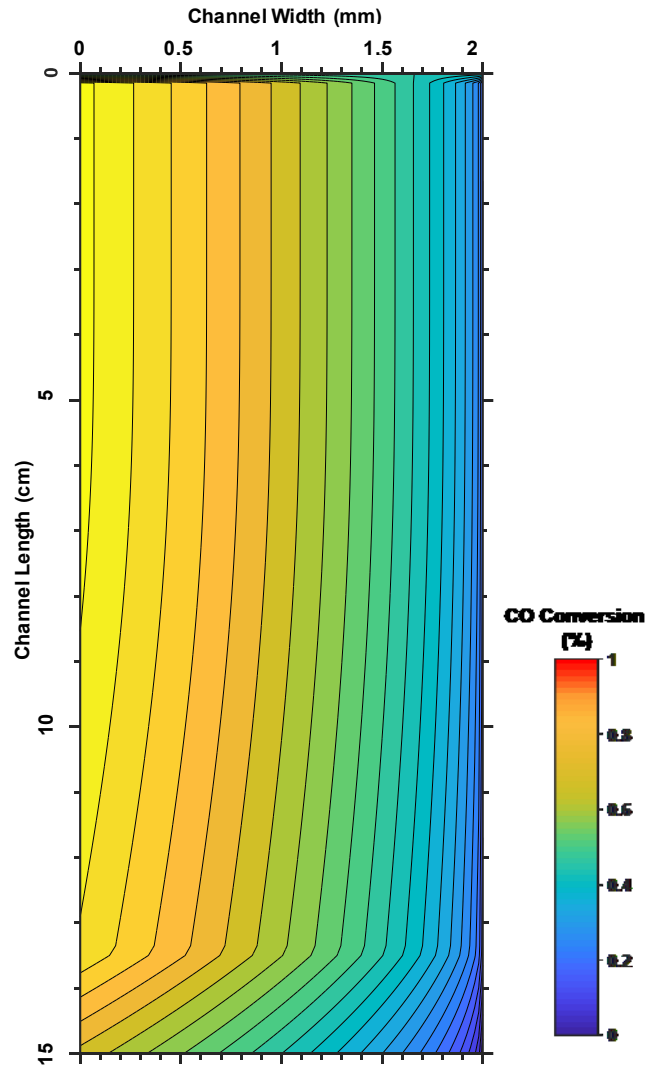
Figure 28: Contours for CO conversion along the packed channel at u = 0.15 m/s

4.3.3   Effect of H_2/CO ratio on CO Conversion

Figures 28 and 29 show the 2-D model predictions of the effect of H_2/CO ratio on the CO conversion in the packed channel at a superficial gas velocity of 0.01 m/s. When compared to Figure 20, which represents the results corresponding to $H_2/CO = 2$, increasing the H_2/CO ratio (Figure 29) slightly increases the conversion throughout the packed channel. However, when the

H$_2$/CO ratio is decreased, a significant decrease of CO conversion can be observed throughout the packed channel. These results can be attributed to the fact that H$_2$ is the limiting reactant in F-T synthesis with Co catalyst, and accordingly higher H$_2$/CO ratios should increase the CO conversion, whereas lower H$_2$/CO ratios significantly decrease the CO conversion, due to lack of hydrogen.
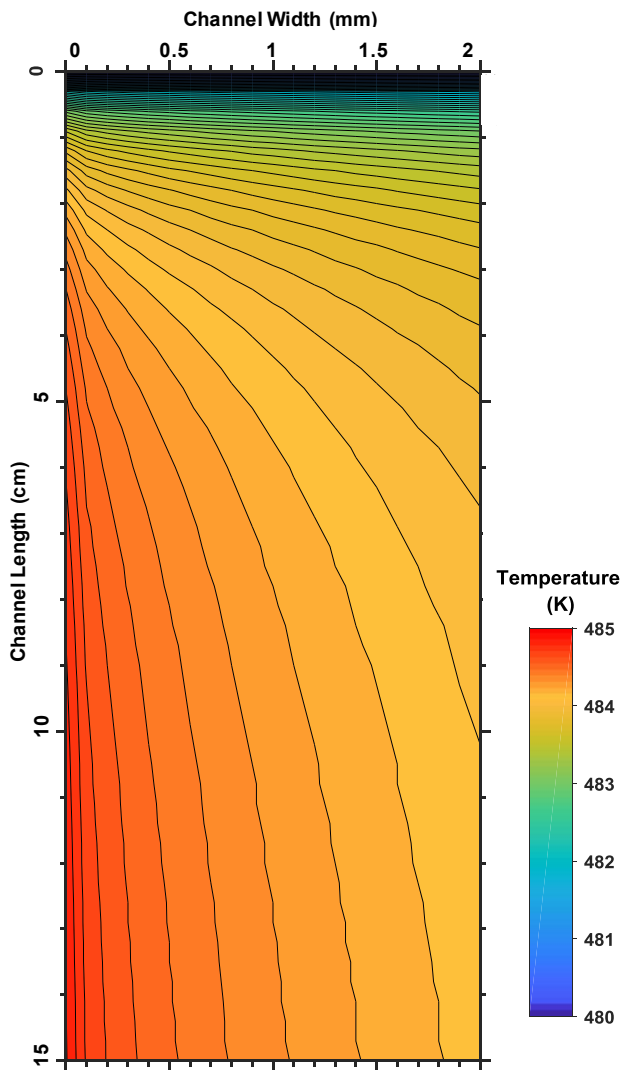
Figure 29: Contours for CO conversion along the channel at H$_2$/CO of 2.2
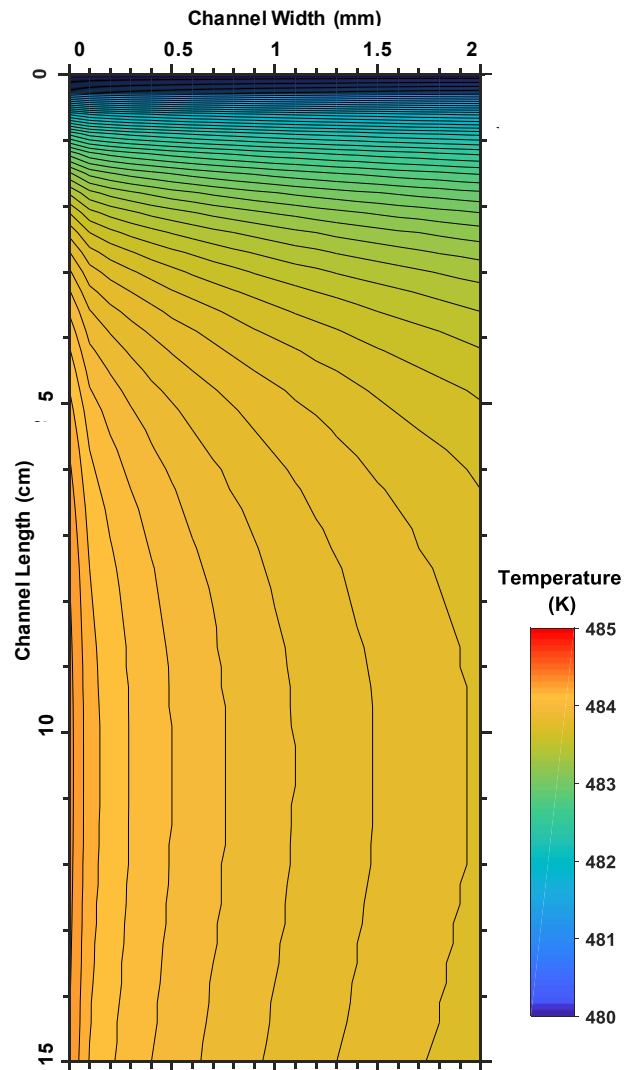
Figure 30: Contours for CO conversion along the channel at H$_2$/CO of 1.5

4.3.4 Estimating reactor productivity

The molar flow rates of the products at the outlet of the reactor were determined, using a 2-α probability distribution model, as described in Section 3.4. The C_{5+} reactor productivity was subsequently determined for a MCR with dimensions of 160 mm x 360 mm x 150 mm, which corresponds to 3600 packed channels. The yield was estimated to be 3.84 bbl/day when operating with a superficial gas velocity of 0.05 m/s at P = 25 bar, T = 483 K and H_2/CO ratio of 2, the reactor productivity increased with decreasing the superficial gas velocity and was determined to be 4.2 bbl/day.

5.0   CONCLUSIONS

In this study, stress analysis calculations and modeling of a MCR for F-T synthesis were carried out. Two-dimensional (2-D) and three-dimensional (3-D) models were used for stress analysis calculations in a MCR containing 10 channels with dimensions of 10 mm x 185 mm x 500 mm provided with a 10-mm diameter hole for gas entrance and a 10-mm as vent. The analyses, including total deformations, von Mises stresses and the principal stresses, were calculated with ANSYS static structural model using the Finite Element Method. Two different construction materials for the MCR, namely Plexiglas and 316 Stainless Steel were considered in the calculations. Subsequent to the stress analyses, a 2-D pseudo-homogeneous axial and lateral dispersion model was built to investigate F-T synthesis using cobalt catalyst reaction kinetics in the MCR. The effects of superficial gas velocity and H_2/CO ratio on the temperature distribution and the MCR performance were predicted. The stress analyses and modeling efforts led to the following conclusions:

1. The 2-D stress analysis model systematically predicted the failure of the MCR inlet surface by evaluating the elastic plastic fracture mechanics of the structure. The maximum allowable load was determined for both smooth and crack induced inlet surface.

2. The 3-D stress analysis included the addition of boundary and loading conditions on the complete MCR parts. Areas of the maximum and minimum stress were determined assuming different loading conditions, such as pressure, force and displacement. Stress contours for the

59

inlet box, channels and the complete MCR body were produced. The 3-D stress analysis results showed that the maximum stresses exhibited within the structure were generally lower than the maximum yield strength of both Plexiglas and Stainless steel. The Plexiglas structure was found to be able to withstand a maximum pressure of 4 atm., however, it is unlikely to operate at such a limit due to safety considerations.

3. Increasing the inlet superficial gas velocity decreased the CO conversion and the temperature distribution in the MCR. The highest CO conversion and temperature values were exhibited at the centerline of the reactor. The temperature gradients decreased significantly with increasing superficial gas velocity.

4. Decreasing the H_2/CO ratio of the feed systematically decreased the CO conversion throughout the packed-channel, whereas increasing the H_2/CO ratio resulted in higher and steeper CO conversion contours.

5. The hydrocarbons yield was determined to be 3.84 bbl/day for 3600 channels with dimensions of 4 mm x 4 mm x 150 mm operating at P = 25 bar, T = 483 K, H_2/CO ratio of 2, and a superficial inlet velocity of 0.05 m/s, the yield was also determined to be 4.24 bbl/day when operating at a superficial velocity of 0.01 m/s.

APPENDIX A

STRESS THEORIES FOR MECHANICAL DESIGN

A.1 STATE OF STRESS AT A POINT

The three most important parameters in mechanical design are stress, strain, and energy. If a body were to be cut by an arbitrary plane, these parameters would be distributed continuously over the surface and would vary in both direction and intensity. Furthermore, the internal force distribution would also be a function of the orientation of the plane [52].

Stress is the term used to define the intensity and direction of the internal forces acting at a given point on a particular plane. Figure 31 shows the completely defined state of stress on an elemental volume of dimensions dx, dy, and dz. Normal stresses are called positive when they produce tension and negative when they produce compression.
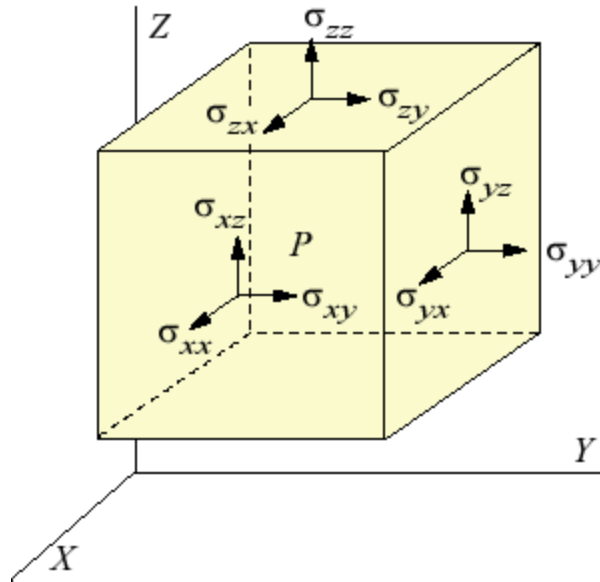
Figure 31: State of stress at a point

A.2 PRINCIPAL STRESSES

Principal normal stresses, sometimes called simple principal normal stresses are the normal stresses that occur on the plane where the shearing stresses are zero. The planes on which the principal normal stresses act are called principal planes. The principal normal stresses are also the local extremes of the stress that include the maximum value of normal stress that can occur on any plane through the point. Since failure moduli are often related to the principal stresses or to the maximum principal stress, they are computed in this work using ANSYS Mechanical solver for the micro channel reactor assembly and individual parts [52, 72].

There are three principal stresses: the 1st principal stress gives you the value of stress that is normal to the plane in which the shear stress is zero. The 1st principal stress helps you understand the

maximum tensile stress induced in the part due to the loading conditions. The 3rd principal stress acts normal to the plane in which shear stress is zero. The following equations determine the three normal principal stresses [73, 74]:

$$\sigma_1 = \sigma_{x'}$$

$$\sigma_2 = \frac{\sigma_{y'} + \sigma_{z'}}{2} + \sqrt{\left(\frac{\sigma_{y'} - \sigma_{z'}}{2}\right)^2 + \sqrt{\tau_{y'z'}^2}} \qquad \text{(B-1)}$$

$$\sigma_3 = \frac{\sigma_{y'} + \sigma_{z'}}{2} - \sqrt{\left(\frac{\sigma_{y'} - \sigma_{z'}}{2}\right)^2 + \sqrt{\tau_{y'z'}^2}}$$

And the principal shearing stresses are determined by equation 1.2-2:

$$\tau_1 = \pm\frac{1}{2}(\sigma_2 - \sigma_3) \qquad \text{(B-2)}$$

$$\tau_2 = \pm\frac{1}{2}(\sigma_1 - \sigma_3) \qquad \text{(B-3)}$$

$$\tau_3 = \pm\frac{1}{2}(\sigma_1 - \sigma_2) \qquad \text{(B-4)}$$

A.3 CONCEPT OF ENGINEERING STRESS-STRAIN

Engineering stress is defined to be the force per unit of original cross - sectional area

$$S = \frac{P}{A_o} \tag{B-5}$$

Where S is engineering stress, P is the applied load and A_o is the original cross-sectional area normal to P in a simple tensile test. Similarly, engineering strain, or nominal strain is defined as the elongation per unit of original length,

$$\varepsilon = \frac{\Delta l}{l_o} \tag{B-6}$$

Where ε is engineering strain, Δl is the change in gage length under load, and l_o is the original gage length prior to application of the load [52, 75].

A.4 ELASTIC STRESS-STRAIN RELATIONSHIPS

Collins [52] well defines the linear relationship between stress and strain in the elastic range for homogeneous and isotropic engineering materials experimentally. Three equations are deduced which relate normal strains to the applied normal stresses which are known as Hook's law equations[76]:

$$\epsilon_1 = \frac{1}{E}[\sigma_1 - v(\sigma_2 + \sigma_3)] \tag{B-7}$$

$$\epsilon_2 = \frac{1}{E}[\sigma_2 - v(\sigma_1 + \sigma_3)]$$

$$\epsilon_3 = \frac{1}{E}[\sigma_3 - v(\sigma_1 + \sigma_2)]$$

Where v is the material constant called Poisson's ratio [77].

A.5 PLASTIC STRESS- STRAIN RELATIONSHIPS

Since structures are sometimes operated beyond the yield point, it is important to investigate the stress-strain relationships in the plastic range where the linear elastic relationships are no longer applicable. The stress strain relationships in the plastic region are generally not independent of time. Any exact theory of plastic deformation should take into account the entire history of deformation from the time plastic flows was initiated [52, 78]. Such relationships would be complex, involving the stress and the time rate of strain. The equations are analogous to the equations for flow of a viscous fluid, and the strain at any given time would be determined through a step by step integration over the entire strain history [79].

$$\delta_1 = \frac{2C_i}{3}\left[\sigma_1 - \frac{1}{2}(\sigma_2 + \sigma_3)\right]$$

$$\delta_2 = \frac{2C_i}{3}\left[\sigma_2 - \frac{1}{2}(\sigma_1 + \sigma_3)\right] \qquad (B\text{-}8)$$

$$\delta_3 = \frac{2C_i}{3}\left[\sigma_3 - \frac{1}{2}(\sigma_1 + \sigma_2)\right]$$

Where $\delta = \ln(1 + \varepsilon)$ and $C_i = \frac{\delta_1 - \delta_2}{\sigma_1 - \sigma_2} = \frac{\delta_2 - \delta_3}{\sigma_2 - \sigma_3} = \frac{\delta_3 - \delta_1}{\sigma_3 - \sigma_1}$

A.6   COMBINED STRESS THEORIES OF FAILURE

If an equipment or its part under consideration is subjected to a biaxial or a triaxial state of stress, prediction of failure is more difficult and we cannot predict yielding. The maximum normal stress reaches the tensile yield point because the other normal stress components may also influence yielding. A large number of complex multiaxial tests would be required in which all of the stress components would be varied over their entire range of values in all possible combinations, and even then it would be difficult to assess the influence of outside factors such as stress concentrations, temperature and environment [52, 80].

The basic assumption for all combined stress failure theories is that failure is predicted to occur when the maximum value of the selected mechanical modulus in the multiaxial state of stress becomes equal to or exceeds the value of the same modulus that produces failure in a simple uniaxial stress test using the same material [52, 81].

To summarize, the development of any useful combined stress failure theory must contain three essential ingredients proposed by Collins work [52].

1. It should provide an applicable model, described by mathematical relationships that relates the external loading to the stresses, strains or other calculable mechanical moduli at the critical point in the multiaxial state of stress.

2. It must be based on critical physical properties of the material that are measurable.

3. It must relate the calculable mechanical modulus in the multi axial state of stress to a measurable criteria of failure based on the critical measurable properties determined in a simple uniaxial test [52, 82]

Six of these combined stress failure theories are described in Table 10.

66

Table 10: Combined Stress theories of failure

Type / Description	Failure Criteria Equations
Maximum Normal Stress theory (Rankine's Theory): Failure is predicted to occur in the multiaxial state of stress when the maximum principal normal stress becomes equal to or exceeds the maximum normal stress at the time of failure in a simple uniaxial stress test using a specimen of same material[83] .	$\sigma_1 \geq \sigma_t; \sigma_2 \geq \sigma_t; \sigma_3 \geq \sigma_t$ $\sigma_1 \leq \sigma_c; \sigma_2 \leq \sigma_c; \sigma_3 \leq \sigma_c$
Maximum shearing stress theory (Tresca-guest theory): Failure is predicted to occur in the multiaxial state of stress when the maximum shearing stress magnitude becomes equal to or exceeds the maximum shearing stress magnitude at the time of failure in a simple uniaxial stress test using a specimen of same material [84].	$\|\sigma_1 - \sigma_2\| \geq \|\sigma_f\|$
Total strain energy theory (Beltrami theory): Failure is predicted to occur in the multiaxial state of stress when the total strain energy per unit volume becomes equal to or exceeds the total strain energy per unit volume at the time of failure in a simple uniaxial stress test using a specimen of same material [85]. This theory is feasible for ductile materials.	$[\sigma_1^2 + \sigma_2^2 + \sigma_3^2 - 2v(\sigma_1\sigma_2 + \sigma_2\sigma_3 + \sigma_3\sigma_1)] \geq \sigma_f^2$
Maximum normal strain theory (St. Venant's theory): Failure is predicted to occur in the multiaxial state of stress when the maximum principal normal strain becomes equal to or exceeds the maximum normal strain at the time of failure in a simple uniaxial stress test using the specimen of the same material [52, 86]	$\sigma_1 - v(\sigma_2 + \sigma_3) \geq \sigma_f \; ; \; \sigma_1 - v(\sigma_2 + \sigma_3) \leq -\sigma_f$
Distortion Energy theory (Huber-Von Mises-Hencky theory: Failure is predicted to occur in the multiaxial state of stress when the distortion energy per unit volume at the time of failure in a simple uniaxial stress test using a specimen of the same material [52, 87].	$\frac{1}{2}[(\sigma_1 - \sigma_2)^2 + (\sigma_2 - \sigma_3)^2 + (\sigma_3 - \sigma_1)^2] \geq \sigma_f^2$
Mohr's Failure theory: Failure is predicted to occur in the multiaxial state of stress when the largest Mohr's circle associated with the state of stress at a given critical point becomes tangent to or exceeds the bounds of the failure envelope determined from the conditions of failure in simple tensile, compressive and torsion tests using species of the same material [52, 88].	Radii of the three circles are: $R_1 = \dfrac{\sigma_2 - \sigma_3}{2}; R_2 = \dfrac{\sigma_1 - \sigma_3}{2}; R_3 = \dfrac{\sigma_1 - \sigma_2}{2}$

A.7 FINITE ELEMENT METHOD TO COMPUTE STRESSES

The Finite element method is a numerical procedure that can be applied to obtain solutions to a variety of problems in engineering. Steady, transient, linear or nonlinear problems in stress analysis, heat transfer, fluid flow, and electromagnetism problems may be analyzed with the FEM [55]. Ansys is a comprehensive general-purpose finite element computer program that contains over 100,000 lines of code. ANSYS can perform static, dynamic, heat transfer, fluid flow, and electromagnetism analyses. Basic steps in the FEM consist of Preprocessing phase which includes creation and discretization of the solution domain into finite elements which means to subdivide the problem into nodes and elements, develop equations for an element and apply boundary conditions and loading. The second step include solution phase and post-processing phase in which a set of linear or non-linear algebraic equations are solved simultaneously to obtain the nodal results such as displacement values at different nodes or temperature values at different nodes in a heat transfer problem. Lastly, in the post processing phase, other important information is obtained such as values of principal stresses, heat fluxes etc. using the displacement value obtained in FEM [55, 89].

FEM can be applied to a general matrix equation:

$$\{Reaction\ Matrix\} = \{stiffness\ matrix\}\{displacement\ matrix\} - \{load\ matrix\}$$

In general, there are several approaches to formulating FEM problems like direct formulation, minimum total energy formulation and weighted residual formulations [55].

BIBLIOGRAPHY

[1]   N. Hargreaves, "Roll out of smaller scale GTL technology at ENVIA Energy's plant in Oklahoma City, USA," presented at the Gastech, Tokyo, Japan, 2017.

[2]   G. Kolb and V. Hessel, "Micro-structured reactors for gas phase reactions," *Chemical Engineering Journal,* vol. 98, pp. 1-38, 2004.

[3]   R. B. Bird, W. E. Stewart, and E. N. Lightfoot, *Transport Phenomena*: Wiley, 2007.

[4]   A. Oroskar, K. Van den Bussche, and S. Abdo, "Intensification in Microstructured Unit Operations Performance Comparison Between Mega and Micro Scale," in *Microreaction Technology*, M. Matlosz, W. Ehrfeld, and J. Baselt, Eds., ed: Springer Berlin Heidelberg, 2001, pp. 153-163.

[5]   M. J. Matlosz, W. Ehrfeld, and J. P. Baselt, *Microreaction Technology: Proceedings of the Fifth International Conference on Microreaction Technology ; with 41 Tables*: Springer, 2002.

[6]   H. Tomlinson, E. Roth, and K. Agee, "Movable gas-to-liquid system and process," ed: Google Patents, 2004.

[7]   T. Jarosch Kai, Y. Tonkovich Anna Lee, T. Perry Steven, D. Kuhlmann, and Y. Wang, "Microchannel Reactors for Intensifying Gas-to-Liquid Technology," in *Microreactor Technology and Process Intensification*. vol. 914, ed: American Chemical Society, 2005, pp. 258-272.

[8]   C. Cao, M. Liu, J. Wen, and Q. Guo, "Experimental measurement and numerical simulation for liquid flow velocity and local phase hold-ups in the riser of a GLSCFB," *Chemical Engineering and Processing: Process Intensification,* vol. 48, pp. 288-295, 2009.

[9]   R. Myrstad, S. Eri, P. Pfeifer, E. Rytter, and A. Holmen, "Fischer–Tropsch synthesis in a microstructured reactor," *Catalysis Today,* vol. 147, Supplement, pp. S301-S304, 2009.

[10]   J. Knochen, R. Güttel, C. Knobloch, and T. Turek, "Fischer–Tropsch synthesis in milli-structured fixed-bed reactors: Experimental study and scale-up considerations," *Chemical Engineering and Processing: Process Intensification,* vol. 49, pp. 958-964, 2010.

[11]   C. Knobloch, R. Güttel, and T. Turek, "Holdup and Pressure Drop in Micro Packed-Bed Reactors for Fischer-Tropsch Synthesis," *Chemie Ingenieur Technik,* vol. 85, pp. 455-460, 2013.

[12]   C. L. Penniall, "Fischer-Tropsch Based Biomass to Liquid Fuel Plants in the New Zealand Wood Processing Industry Based on Microchannel Reactor Technology," 2013.

[13]   P. Piermartini, T. Schuhmann, P. Pfeifer, and G. Schaub, "Water Gas Shift in Microreactors at Elevated Pressure: Platinum-Based Catalyst Systems and Pressure Effects," *Topics in Catalysis,* vol. 54, pp. 967-976, 2011/09/01 2011.

[14]   P. Pfeifer, K. Schubert, M. A. Liauw, and G. Emig, "Electrically Heated Microreactors for Methanol Steam Reforming," *Chemical Engineering Research and Design,* vol. 81, pp. 711-720, 2003.

[15]   A. Karim, J. Bravo, D. Gorm, T. Conant, and A. Datye, "Comparison of wall-coated and packed-bed reactors for steam reforming of methanol," *Catalysis Today,* vol. 110, pp. 86-91, 2005.

[16]   M. T. Janicke, H. Kestenbaum, U. Hagendorf, F. Schüth, M. Fichtner, and K. Schubert, "The Controlled Oxidation of Hydrogen from an Explosive Mixture of Gases Using a Microstructured Reactor/Heat Exchanger and Pt/Al2O3 Catalyst," *Journal of Catalysis,* vol. 191, pp. 282-293, 2000.

[17]   H. Ge, G. Chen, Q. Yuan, and H. Li, "Gas phase catalytic partial oxidation of toluene in a microchannel reactor," *Catalysis Today,* vol. 110, pp. 171-178, 2005.

[18]   S. Walter, S. Malmberg, B. Schmidt, and M. A. Liauw, "Mass transfer limitations in microchannel reactors," *Catalysis Today,* vol. 110, pp. 15-25, 2005.

[19]   I. Aartun, H. J. Venvik, A. Holmen, P. Pfeifer, O. Görke, and K. Schubert, "Temperature profiles and residence time effects during catalytic partial oxidation and oxidative steam reforming of propane in metallic microchannel reactors," *Catalysis Today,* vol. 110, pp. 98-107, 2005/12/15/ 2005.

[20]   Y. Su, Y. Zhao, F. Jiao, G. Chen, and Q. Yuan, "The intensification of rapid reactions for multiphase systems in a microchannel reactor by packing microparticles," *AIChE Journal,* vol. 57, pp. 1409-1418, 2011.

[21]   P. Pfeifer, K. Schubert, M. Liauw, and G. Emig, "Electrically heated microreactors for methanol steam reforming," *Chemical Engineering Research and Design,* vol. 81, pp. 711-720, 2003.

[22]   D. Nemec and J. Levec, "Flow through packed bed reactors: 2. Two-phase concurrent downflow," *Chemical Engineering Science,* vol. 60, pp. 6958-6970, 2005/12/01/ 2005.

[23]   B. Schmidt and M. Liauw, "Mass transfer limitations in microchannel reactors," *Catalysis today,* vol. 110, pp. 15-25, 2005.

[24]   S. Walter, S. Malmberg, B. Schmidt, and M. A. Liauw, "Comparison of Microchannel and Fixed Bed Reactors for Selective Oxidation Reactions: Isoprene to Citraconic Anhydride," *Chemical Engineering Research and Design,* vol. 83, pp. 1019-1029, 2005/08/01/ 2005.

[25]   G. Veser, "Process Intensification through Heat-Integration for High-Temperature Catalysis," in *Microreactor Technology and Process Intensification*. vol. 914, ed: American Chemical Society, 2005, pp. 145-161.

[26]   O. Flögel, J. D. C. Codée, D. Seebach, and P. H. Seeberger, "Microreactor Synthesis of β-Peptides," *Angewandte Chemie International Edition,* vol. 45, pp. 7000-7003, 2006.

[27]   R. Halder, A. Lawal, and R. Damavarapu, "Nitration of toluene in a microreactor," *Catalysis today,* vol. 125, pp. 74-80, 2007.

[28]   Y. Men, G. Kolb, R. Zapf, H. Pennemann, and V. Hessel, "Total combustion of propane in a catalytic microchannel combustor," *Chemical Engineering Research and Design,* vol. 87, pp. 91-96, 2009/01/01/ 2009.

[29]   R. Myrstad, S. Eri, P. Pfeifer, E. Rytter, and A. Holmen, "Fischer–Tropsch synthesis in a microstructured reactor," *Catalysis Today,* vol. 147, pp. S301-S304, 2009.

[30]   S. R. Deshmukh, A. L. Y. Tonkovich, K. T. Jarosch, L. Schrader, S. P. Fitzgerald, D. R. Kilanowski*, et al.*, "Scale-Up of Microchannel Reactors For Fischer−Tropsch Synthesis," *Industrial & Engineering Chemistry Research,* vol. 49, pp. 10883-10888, 2010/11/03 2010.

[31]   P. Piermartini and P. Pfeifer, "Microreactor Approaches for Liquid Fuel Production from Bioderived Syngas −5 m3/h Prototype Development for HTHP Water Gas Shift," *Industrial & Engineering Chemistry Research,* vol. 54, pp. 4561-4571, 2015/04/29 2015.

[32]   P. F. Schubert, "Development of larger FT reactors & progress at ENVIA Energy's GTL plant," in *EFI Gas-to-Market & Energy Conversion Forum,* Hotel Granduca, Houston, Texas, 2016.

[33]   B. I. Morsi and O. Basha, "Indirect Coal Liquefaction," Antalyia, Turkey, 2014.

[34]   J. McDaniel. (2015, The future of GTL.

[35]   Z. Liu, S. Shi, and Y. Li, "Coal liquefaction technologies—Development in China and challenges in chemical reaction engineering," *Chemical Engineering Science,* vol. 65, pp. 12-17, 2010.

[36]   D. A. Wood, C. Nwaoha, and B. F. Towler, "Gas-to-liquids (GTL): A review of an industry offering several routes for monetizing natural gas," *Journal of Natural Gas Science and Engineering,* vol. 9, pp. 196-208, 2012.

[37]   A. de Klerk, *Fischer-Tropsch Refining*. Weinheim: Wiley-VCH Verlag & Co. KGaA, 2012.

[38]   T. G. Kreutz, E. D. Larson, G. Liu, and R. H. Williams, "Fischer-Tropsch fuels from coal and biomass," in *25th Annual International Pittsburgh Coal Conference,* 2008.

[39]   A. de Klerk and E. Furimsky, *Catalysis in the Refining of Fischer-Tropsch Syncrude*: Royal Society of Chemistry, 2010.

[40]   M. Dry, "The fischer-tropsch process-commercial aspects," *Catalysis today,* vol. 9570, 1990.

[41]   M. E. Dry, "The Fischer-Tropsch process: 1950-2000," *Catalysis Today,* vol. 71, pp. 227-241, 2002.

[42]   B. Bao, M. M. El-Halwagi, and N. O. Elbashir, "Simulation, integration, and economic analysis of gas-to-liquid processes," *Fuel Processing Technology,* vol. 91, pp. 703-713, 2010.

[43]   M. Sudiro and A. Bertucco, "Production of synthetic gasoline and diesel fuel by alternative processes using natural gas and coal: Process simulation and optimization," *Energy,* vol. 34, pp. 2206-2214, 2009.

[44]   L. Sehabiague, O. Basha, and B. I. Morsi, "Recycling of Tail Gas in Fischer-Tropsch Bubble Column Slurry Reactor and its Impact on the Coal-to-Liquid Process," presented at the Proceedings of the 30th Annual International Pittsburgh Coal Conference, Beijing, China, 2013.

[45]   R. L. Espinoza, a. P. Steynberg, B. Jager, and a. C. Vosloo, "Low temperature Fischer–Tropsch synthesis from a Sasol perspective," *Applied Catalysis A: General,* vol. 186, pp. 13-26, 1999.

[46]   L. Sehabiague, "Modeling, Scaleup and Optimization of Slurry Bubble Column Reactors for Fischer-Tropsch Synthesis," Doctoral Dissertation, Department of Chemical and Petroleum Engineering, University of Pittsburgh, 2012.

[47]   R. Chedid, M. Kobrosly, and R. Ghajar, "The potential of gas-to-liquid technology in the energy market: The case of Qatar," *Energy Policy,* vol. 35, pp. 4799-4811, 2007.

[48]   D. Gray, A. Elsawy, G. Tomlinson, G. J. Stiegel, and R. D. Srivastava, *Proceedings of the DOE Liquefaction Contractors' Review Meeting,* p. 344, 1991.

[49]   L. P. D. a. Fabricators. Technical Data Sheet Plexiglass (PMMA) [Online]. Available: http://www.laminatedplastics.com/plexiglass.pdf

[50]   M.   M.   P.   Data.   Available: http://www.matweb.com/search/datasheet.aspx?bassnum=O1303&ckck=1

[51]   A. Materials, "Material:Stainless Steel - grade 316 (UNS S31600)."

[52]   J. A. Collins, *Failure of materials in mechanical design*: John Wiley & sons, Inc., 1981.

[53]   J. A. Collins, *Failure of materials in mechanical design: analysis, prediction, prevention*: John Wiley & Sons, 1993.

[54]   I. Demirdžić and S. Muzaferija, "Finite volume method for stress analysis in complex domains," *International Journal for Numerical Methods in Engineering,* vol. 37, pp. 3751-3766, 1994.

[55]   S. Moaveni, "Finite element analysis: theory and application with ANSYS, 1999," *MQ applied force in Y direction bending moment shear force.*

[56]   M. Kutz, *Mechanical Engineers' Handbook, Volume 1: Materials and Engineering Mechanics*: John Wiley & Sons, 2015.

[57]   A. Hillerborg, M. Modéer, and P.-E. Petersson, "Analysis of crack formation and crack growth in concrete by means of fracture mechanics and finite elements," *Cement and concrete research,* vol. 6, pp. 773-781, 1976.

[58]   A. Steynberg and M. Dry, *Fischer-Tropsch Technology*. Amsterdam: Elsevier Science, 2004.

[59]   H. Delmas and G. F. Froment, "A SIMULATION MODEL ACCOUNTING FOR STRUCTURAL RADIAL NONUNIFORMITIES IN FIXED BED REACTORS. A2 - BOURNE, J.R," in *Tenth International Symposium on Chemical Reaction Engineering*, W. Regenass and W. Richarz, Eds., ed: Pergamon, 1988, pp. 2281-2287.

[60]   B. Todic, M. Mandic, N. Nikacevic, and D. B. Bukur, "Effects of process and design parameters on heat management in fixed bed Fischer-Tropsch synthesis reactor," *Korean Journal of Chemical Engineering,* February 15 2018.

[61]   N. Park, J.-R. Kim, Y. Yoo, J. Lee, and M.-J. Park, "Modeling of a pilot-scale fixed-bed reactor for iron-based Fischer–Tropsch synthesis: Two-dimensional approach for optimal tube diameter," *Fuel,* vol. 122, pp. 229-235, 2014.

[62]   O. J. Catchpole, R. Bernig, and M. B. King, "Measurement and Correlation of Packed-Bed Axial Dispersion Coefficients in Supercritical Carbon Dioxide," *Industrial & Engineering Chemistry Research,* vol. 35, pp. 824-828, 1996/01/01 1996.

[63]   D. Gunn, "On axial dispersion in fixed beds," *Chemical Engineering and Processing: Process Intensification,* vol. 32, pp. 333-338, 1993.

[64]   C. S. Tan and D. C. Liou, "Axial dispersion of supercritical carbon dioxide in packed beds," *Industrial & engineering chemistry research,* vol. 28, pp. 1246-1250, 1989.

[65]   E. Tsotsas and E. Schlünder, "On axial dispersion in packed beds with fluid flow: über die axiale dispersion in durchströmten festbetten," *Chemical Engineering and Processing: Process Intensification,* vol. 24, pp. 15-31, 1988.

[66]   V. Sater and O. Levenspiel, "Two-phase flow in packed beds. Evaluation of axial dispersion and holdup by moment analysis," *Industrial & Engineering Chemistry Fundamentals,* vol. 5, pp. 86-92, 1966.

[67]   R. B. Anderson, *Catalysis* vol. 4. New York: P. H. Emmet 1956.

[68]   F. Arias Pinto, "Investigating Microchannel Reactors for Fischer-Tropsch Synthesis," Master's Thesis, Department of Chemical and Petroleum Engineering, University of Pittsburgh, 2016.

[69]   A. Y. Khodakov, W. Chu, and P. Fongarland, "Advances in the development of novel cobalt Fischer− Tropsch catalysts for synthesis of long-chain hydrocarbons and clean fuels," *Chemical reviews,* vol. 107, pp. 1692-1744, 2007.

[70]   B. Todic, T. Bhatelia, G. F. Froment, W. Ma, G. Jacobs, B. H. Davis*, et al.*, "Kinetic Model of Fischer–Tropsch Synthesis in a Slurry Reactor on Co–Re/Al2O3 Catalyst," *Industrial & Engineering Chemistry Research,* vol. 52, pp. 669-679, 2013/01/16 2012.

[71]   H. S. Fogler, *Elements Of Chemical Reaction Engineering*: Prentice Hall Professional Technical Reference, 2006.

[72]   R. D. Cook, *Finite element modeling for stress analysis*: Wiley, 1994.

[73]   H. Fall, "Experimental stress analysis," SAE Technical Paper 0148-7191, 1949.

[74]   E. Hoek, C. Carranza-Torres, and B. Corkum, "Hoek-Brown failure criterion-2002 edition," *Proceedings of NARMS-Tac,* vol. 1, pp. 267-273, 2002.

[75]   Y. Murakami, "Stress intensity factors," 1987.

[76]   W. T. Koiter, "Stress-strain relations, uniqueness and variational theorems for elastic-plastic materials with a singular yield surface," *Quarterly of applied mathematics,* vol. 11, pp. 350-354, 1953.

[77]   M. Asmani, C. Kermel, A. Leriche, and M. Ourak, "Influence of porosity on Young's modulus and Poisson's ratio in alumina ceramics," *Journal of the European ceramic society,* vol. 21, pp. 1081-1086, 2001.

[78]   J. R. Griffiths and D. J. Owen, "An elastic-plastic stress analysis for a notched bar in plane strain bending," *Journal of the Mechanics and Physics of Solids,* vol. 19, pp. 419-431, 1971.

[79]   R. M. Richard and B. J. Abbott, "Versatile elastic-plastic stress-strain formula," *Journal of the Engineering Mechanics Division,* vol. 101, pp. 511-515, 1975.

[80]   T. Matake, "An explanation on fatigue limit under combined stress," *Bulletin of JSME,* vol. 20, pp. 257-263, 1977.

[81]   R. J. Roark, "Formulas for stress and strain," 1954.

[82]   W. Cui and M. Wisnom, "A combined stress-based and fracture-mechanics-based model for predicting delamination in composites," *Composites,* vol. 24, pp. 467-474, 1993.

[83]   J. Byerlee, "Friction of rocks," in *Rock friction and earthquake prediction*, ed: Springer, 1978, pp. 615-626.

[84]   R. E. Wallace, "Geometry of shearing stress and relation to faulting," *The Journal of Geology,* vol. 59, pp. 118-130, 1951.

[85]   K. Golos and F. Ellyin, "A total strain energy density theory for cumulative fatigue damage," *Journal of pressure vessel technology,* vol. 110, pp. 36-41, 1988.

[86]   K. J. Chang, "On the maximum strain criterion—a new approach to the angled crack problem," *Engineering Fracture Mechanics,* vol. 14, pp. 107-124, 1981.

[87]   Y. M. Xie and G. P. Steven, "A simple evolutionary procedure for structural optimization," *Computers & structures,* vol. 49, pp. 885-896, 1993.

[88]   G. E. Dieter and D. J. Bacon, *Mechanical metallurgy* vol. 3: McGraw-hill New York, 1986.

[89]   G. Dhatt, E. LefranÃ, and G. Touzot, *Finite element method*: John Wiley & Sons, 2012.